**BABEŞ-BOLYAI UNIVERSITY OF CLUJ-NAPOCA
FACULTY OF CHEMISTRY AND CHEMICAL
ENGINEERING
DOCTORAL SCHOOL OF CHEMISTRY**

IOANA MIHAELA PERHAIŢA

NEW APATITE SILICATES WITH LUMINESCENT AND ELECTRICAL PROPERTIES

PhD Thesis Summary

**SCIENTIFIC SUPERVISOR
Prof. Dr. LIANA MARIA MUREŞAN**

2021

BABEŞ-BOLYAI UNIVERSITY OF CLUJ-NAPOCA
FACULTY OF CHEMISTRY AND CHEMICAL ENGINEERING
DOCTORAL SCHOOL OF CHEMISTRY

IOANA MIHAELA PERHAIŢA

NEW APATITE SILICATES WITH LUMINESCENT AND ELECTRICAL PROPERTIES

PhD Thesis Summary

<u>Scientific supervisor:</u>
Prof. Dr. Liana Maria Mureşan, *Babeş-Bolyai University* of Cluj-Napoca*, Faculty of Chemisty and Chemical Engineering*
Chairman of the committee:
Prof. Dr. Eng. Monica Toşa, *Babeş-Bolyai University* of Cluj-Napoca*, Faculty of Chemisty and Chemical Engineering*
Reviewers:
Prof. Dr. Eng. Nicolae Vaszilcsin - *Polytechnic University* of Timişoara, *Faculty of Chemistry and Environmental Engineering*
Prof. Dr. Ionel Chicinaş - *Technical University* of Cluj-Napoca, *Faculty of Materials and Environmental Engineering*
Assoc. Prof. Dr. Eng. Firuţa Goga - *Babeş-Bolyai University* of Cluj-Napoca, *Faculty of Chemisty and Chemical Engineering*

2021

THESIS CONTENT

ABBREVIATIONS

BET	**B**runauer-**E**mmett-**T**eller method
BJH	**B**arett-**J**oyner-**H**alenda method
C	**C**ombustion
D_{ef}	the average size of the crystallites
DTA	**D**ifferential **T**hermal **A**nalysis
DTG	**D**erivative **T**hermo**G**ravimetry
EDX	**E**nergy **D**ispersive **X**-ray Spectroscopy
EGA	**E**volved **G**as **A**nalysis
EIS	**E**lectrochemical **I**mepdance **S**pectroscopy
FT-IR	**F**ourier **T**ransformed **I**nfra**R**ed Spectroscopy
ICP-OES	**I**nductiv **C**oupled **P**lasma-**O**ptical **E**mission **S**pectrometry
ICSD	**I**norganic **C**rystal **S**tructure **D**atabase
IUPAC	**I**nternational **U**nion of **P**ure and **A**pplied **C**hemistry
JCPDS	**J**oint **C**ommission on **P**owder **D**iffraction **S**tandards
LED	**L**ight **E**mitting **D**iode
MT	**T**ranzitional **M**etal
mW	**m**icro**W**ave
NUV	**N**ear**U**ltra**V**iolet
PDF	**P**owder **D**iffraction **F**ile
Pp	**P**reci**p**itation
RE	**R**are **E**arth
RES	**S**pin **E**lectron **R**esonance Spectroscopy
RSS	**S**olid **S**tate **R**eaction
rms	**r**oot **m**ean **s**quare
SEM	**S**canning **E**lectron **M**icroscopy
SOFC	**S**olid **O**xid **F**uel **C**ell
TGA	**T**hermo **G**ravimetric **A**nalysis
XPS	**X**-ray **P**hotoelectron **S**pectroscopy
XRD	**X**-**R**ay **D**iffraction

INTRODUCTION

As a result of the development of investigation methods and the diversification of sinthesys methods, we participate to a real redefinition in the field of materials with special properties. At international level, there is an extraordinary interest to improve the performances of micro- and nano-materials with morpho-structural characteristics and controlled properties. Although the research activity has led to materials that work close to their limits, considerable attention is given to: ►improve the known synthesis methods; ►develop of new materials and new ways of synthesis; ►controll the performance of materials by lowering the particle size towards the nano domain. The apatites class are oxide compounds that can incorporate a variety of cations into the crystal lattice, generating large varieties of compositions. Among the nanocrystalline materials, apatite-type silicates, can successfully function as host lattices for different ions, leading to the obtaining of materials with special properties. For example, by doping with rare earth ions apatites becames luminescent, in the sense that under UV excitation they absorb the radiation and emit light in the visible spectrum with different colors depending on the doping cation. Rare earth ions are preferred due to: ►high probability of short-lived transitions, ►spin allowed transitions, ►low tendency for non-radiative relaxation. On the other hand, by modifying the stoichiometry of apatites and doping with aliovalent cations at different cationic sites of the host lattice, either an interstitial oxygen or vacancies at the predominant cation can be achieved, with implications on the electrical property. The large number of apatite-type compounds that can be obtained fully justifies the experimentation of finding materials with improved luminescent and electrical properties compared to similar materials presented in the literature.

Keywords: apatite, doping ions, solid state reaction, wet synthesis, ionic conductivity, luminescence.

Field of study: nanotechnologies and materials with controlled properties.

Thesis motivation: In the field of nanotechnologies and advanced materials there is a pronounced tendency towards the development of new materials, imposed by the evolution of technologies in areas such as: optoelectronics, efficient lighting, green energy production. Apatites, in addition to great physical and chemical stability, posses the special property to incorporate a variety of cations into the lattice which can lead to substantial changes in their optical and electrical properties bringing variety in the field of materials.

The aim of the thesis: is to obtain new apatite type silicates, with controlled luminescent and electrical properties.

The thesis has specific objectives regarding the synthesis and properties of apatites, as follows:

1) Establishing and optimizing the experimental parameters in different synthesis techniques in order to obtain apatites with controlled morpho-structural, luminescent and electrical characteristics;

2) Characterization of apatites using different specific analysis methods in materials science;

3) Compositional design of materials taking into account the optimal fit of the cations involved in the apatite lattice;

4) Comparative study of the luminescent properties of apatites according to the experimental conditions; establishing correlations between the synthesis method and the properties of the material; elucidation of the energy transfer involved in luminescence; the role of cations in the luminescence process; estimation of possible applications;

5) Studies on ionic conductivity in various compositions by doping the apatite lattice with different cations.

The scientific novelty and originality refers to: *the identification of the experimental parameters that ensure to obtain pure structural apatites by the *Solid State Reaction* and by the *Precipitation* method; *obtaining by *Combustion* of one apatite with improved conductivity in comparison with literature; *optimization of preparative conditions for apatites by *Precipitation* through: pH, reactants concentration and calcination temperature; *obtaining improved luminescent characteristics by *Precipitation* compared to other synthesis methods. Studies on wet synthesis routes led to apatites with improved morpho-structural and luminescent characteristics in comparison to the *Solid State Reaction.*

Aplicative value of the thesis: The silicates with apatite structure have a real applicative potential in various fields: ►efficient lighting systems (lamps, LEDs); ►production of green energy through fuel cells with solid electrolyte, apatite type. The studies developed within the doctoral thesis contribute to the development of knowledge in areas with internationall relevance. The thesis provides new knowledge about the synthesis and optimal preparative conditions of silicates with apatite structure. The new apatites obtained in the thesys posses improved luminescent and electrical properties comparative to similar materials presented in literature. Apatites were characterized by specific analysis techniques and corelations between the synthesis conditions and the morpho-structural characteristics of apatites hawe been made.

Thesis structure: The doctoral thesis is structured in two parts: I- Literature data on the synthesis, properties and applications of silicates with apatite structure; II- Original results regarding new apatite type silicates, with luminescent and electrical properties. The paper contains: 158 pages (basic text), 80 figures, 26 tables. The two parts are structured in 7 chapters, comprised in 202 pages, for editing being consulted 313 bibliographic references, structured on each chapter. The scientific results presented in the thesis are published in 5 papers rated ISI (1-Q1, 2-Q2, 2-Q3 according to Web of Science). The list of papers elaborated on the topic of the thesis can be consulted in ANNEX 6. The first part of the thesis contains 3 chapters that provide information about apatites, types of minerals in the apatite supergroup, crystal structure and types of symmetries. The most used synthesis methods same as the luminescent, electrical properties and requierments that these materials must fulfill for different applications are illustrated. The second part of the thesis is focused on original scientific contributions on the synthesis and characterization of silicates with apatite structure with superior luminescent and electrical properties, being composed of 4 chapters:

▸ Chapter 4- Synthesis methods for apatites with special properties (*Solid State Reaction*, *Precipitation*, *Sol-Gel* and *Combustion)*;

▸ Chapter 5- Influence of the experimental factors on the morpho-structural characteristics of apatite-type silicates. The studies reffers to the effect of thermal treatment (*Solid State Reaction)*; the nature of the precipitating agent; influence of the host lattice; concentration of the reactants and the pH (*Precipitation* method); host lattice and the activator (*Combustion).*

▸ Chapter 6- Luminescent properties of silicates with apatite structure; study of influence: activator, host lattice, synthesis method, pH of the precipitation on the luminescence of $A_x RE_{10-x}(SiO_4)_6 O_{3-x/2}$ apatites, doped with rare earth ions and transitional metals.

▸ Chapter 7- Electrical properties of apatite-type silicates, described by chemical formulas: $La_{10-x} Bi_x(SiO_4)_6 O_3$ (x = 0; 0,1; 0,15; 0,2; 0,3) şi $La_{10}Si_{5,9}MT_{0,1}O_{27\pm\delta}$ (MT = Cr^{3+}, Fe^{3+}, Mn^{4+}, Mo^{6+}, W^{6+}; δ- depends on the oxidation state of the cation).

The Introduction, the General Conclusions, Reagents and analysis techniques together with the Annexes, complete the present paper.

I mention that the research activity was carried out at the "Raluca Ripan" Chemistry Research Institute, Babes-Bolyai University of Cluj-Napoca, Inorganic Compounds Laboratory. Some of the measurements have been made through collaborations with third

institutions: Celal Bayar University of Manisa, Turkey, Faculty of Arts and Sciences, Physics Department (CL); National Institute for Research and Development of Isotopic and Molecular Technologies of Cluj-Napoca, Physics of Nanostructured Systems Department (XRD, SEM, XPS, EDX, RES); Babeş-Bolyai University of Cluj-Napoca, Faculty of Chemistry and Chemical Engineering, Research Center in Electrochemistry and Unconventional Materials (EIS).

PART II

ORIGINAL RESULTS REGARDING NEW APATITE TYPE SILICATES, WITH LUMINESCENT AND ELECTRICAL PROPERTIES

5. Influence of the experimental factors on the morpho-structural characteristics of apatite-type silicates

The preparation of apatite silicates is influenced by various factors, as follows: ►calcination regime, ►precipitating agent, ►pH of precipitation medium, ► reactants ratio, ►the nature of host lattice and activator. Below are presented the results of studies that highlight the role of these parameters on the morphological and structural characteristics of apatites obtained by different synthesis routes.

5.4 pH in precipitation

Due to the complexity of precipitation synthesis, which involves different metal cations (Ca^{2+}, Y^{3+}, Ce^{3+}, Tb^{3+}) with different precipitation rates and solubility products, a control of pH during precipitation is required. For this purpose, precipitation at pH 7, pH 9, pH 11 and free pH with the addition of TEOS in stoichiometric amounts and using a molar excess of 40% was performed. The synthesis conditions are mentioned in Table 5.4.

Table 5.4. Experimental parameters for obtaining apatite by *Precipitation*

Reaction Conditions					Thermal treatment		
Precipit. Agent	Molar ratio Nitrates:TEOS	pH	Activator		Temp. (ºC)	Time (h)	Formula teoretică compus final
			Cations	Conc. (%) *			
NaOH	1 : 0,60	7	Ce - Tb	1,5 - 1,5	1400	4	$Ca_2Y_{7,76}Ce_{0,12}Tb_{0,12}(SiO_4)_6O_2$
NaOH	1 : 0,60	9	Ce - Tb	1,5 - 1,5	1400	4	$Ca_2Y_{7,76}Ce_{0,12}Tb_{0,12}(SiO_4)_6O_2$
NaOH	1 : 0,60	11	Ce - Tb	1,5 - 1,5	1400	4	$Ca_2Y_{7,76}Ce_{0,12}Tb_{0,12}(SiO_4)_6O_2$
NaOH	1 : 0,60	free	Ce - Tb	1,5 - 1,5	1400	4	$Ca_2Y_{7,76}Ce_{0,12}Tb_{0,12}(SiO_4)_6O_2$
NaOH	1 : 0,84	7	Ce - Tb	1,5 - 1,5	1400	4	$Ca_2Y_{7,76}Ce_{0,12}Tb_{0,12}(SiO_4)_6O_2$
NaOH	1 : 0,84	9	Ce - Tb	1,5 - 1,5	1400	4	$Ca_2Y_{7,76}Ce_{0,12}Tb_{0,12}(SiO_4)_6O_2$
NaOH	1 : 0,84	11	Ce - Tb	1,5 - 1,5	1400	4	$Ca_2Y_{7,76}Ce_{0,12}Tb_{0,12}(SiO_4)_6O_2$
NaOH	1 : 0,84	free	Ce - Tb	1,5 - 1,5	1400	4	$Ca_2Y_{7,76}Ce_{0,12}Tb_{0,12}(SiO_4)_6O_2$

reported at 8 moles Y

The evolution of pH during precipitation, together with images of the solutions obtained after the first washing and filtration of the precipitates are shown in Figure 5.20.

The decisive role of pH during precipitation is noticeable. An almost linear course is observed only in the case of precipitation at pH 11 (Figure 5.20.a), an evolution that can ensure the conditions necessary for a complete precipitation of the reactants. At a neutral pH (pH 7), precipitation reaction does not occur completely, in the washing solutions remaining a good part of the cations initially introduced (Figure 5.20.b). The precipitation degree increase with the increasing pH, it can be seen that the washing solution at pH 11 does not contain visible precipitate.
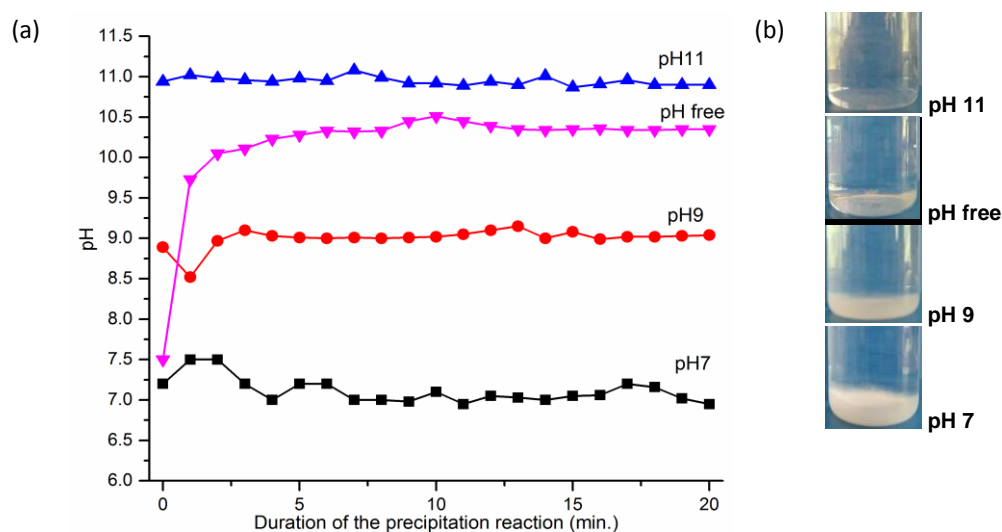
Figure 5.20. pH during precipitation at different times of precipitation reaction (a); solutions resulting from the separation of precipitates after the first wash (b)

The entire evolution of the precipitation was highlighted by the elemental analysis (ICP-OES), which provides data on the distribution of metal ions both in the obtained phosphors and in the maturation and washing solutions of the precipitates.

5.4.1 Elemental analysis

From each residual solution, 50 mL was taken for analysis. 0,05 g of phosphors powders, were weighed and dissolved in a mixture of: nitric acid, sulfuric acid, hydrochloric acid and tetrafluoroboric acid in a ratio of 4: 4: 1: 1, using a Milestone Microwave digester. The as obtained solutions were volumetrically dosed to 100 mL with demineralized water. The detection limits of the elements of interest were as follows: 0,3 μg/L (Y), 0,02 μg/L (Ca), 5 μg/L (Ce), 2 μg/L (Tb). The measurements were made using the ICP-OES method at the

wavelengths specific to each metal, as follows: 371,029 nm (Y), 317,933 (Ca), 413,764 nm (Ce) şi 350,917 nm (Tb). The values obtained from the ICP-OES analysis for the residual solutions were reported to the total volumes of residual solutions and those for the phosphors were reported to the quantities of phosphors obtained from the synthesis. The experimental results are presented in Table 5.5 [28].

Table 5.5. Identified cations (ICP-OES) in phosphors and precipitation/ washing solutions

Sample code	Elemental content (grams)			
	Y	Ca	Ce	Tb
Matured solution				
pH 7	$1,629 \cdot 10^{-3}$	$77,000 \cdot 10^{-3}$	$0,024 \cdot 10^{-3}$	$0,041 \cdot 10^{-3}$
pH 9	$0,184 \cdot 10^{-3}$	$50,000 \cdot 10^{-3}$	$0,004 \cdot 10^{-3}$	$0,006 \cdot 10^{-3}$
pH 11	$0,567 \cdot 10^{-3}$	0,000	$0,029 \cdot 10^{-3}$	$0,018 \cdot 10^{-3}$
pH free	$0,152 \cdot 10^{-3}$	$7,000 \cdot 10^{-3}$	$0,008 \cdot 10^{-3}$	$0,005 \cdot 10^{-3}$
Washing solution I				
pH 7	$0,587 \cdot 10^{-3}$	$8,000 \cdot 10^{-3}$	$0,212 \cdot 10^{-3}$	$0,138 \cdot 10^{-3}$
pH 9	$0,175 \cdot 10^{-3}$	$9,000 \cdot 10^{-3}$	$0,013 \cdot 10^{-3}$	$0,009 \cdot 10^{-3}$
pH11	$0,006 \cdot 10^{-3}$	$0,900 \cdot 10^{-3}$	$0,001 \cdot 10^{-3}$	0,000
pH free	$0,009 \cdot 10^{-3}$	$0,300 \cdot 10^{-3}$	0,000	0,000
Washing solution II				
pH 7	$0,272 \cdot 10^{-3}$	$0,150 \cdot 10^{-3}$	$0,335 \cdot 10^{-3}$	$0,466 \cdot 10^{-3}$
pH 9	$0,328 \cdot 10^{-3}$	$0,400 \cdot 10^{-3}$	$0,011 \cdot 10^{-3}$	$0,020 \cdot 10^{-3}$
pH 11	0,000	$0,550 \cdot 10^{-3}$	$0,001 \cdot 10^{-3}$	0,000
pH free	$0,054 \cdot 10^{-3}$	$0,100 \cdot 10^{-3}$	$0,002 \cdot 10^{-3}$	0,000
Phosphor - 40% TEOS excess				
pH 7	0,702	0,055	0,023	0,023
pH 9	0,956	0,080	0,023	0,031
pH 11	1,132	0,141	0,030	0,033
pH free	1,078	0,138	0,029	0,033
Total cations - experimental *				
pH 7	0,704	0,140	0,024	0,024
pH 9	0,957	0,139	0,023	0,031
pH 11	1,133	0,142	0,030	0,033
pH free	1,078	0,145	0,029	0,033

Cations introduced in precipitation: 1,240 g Y^{3+}; 0,144 g Ca^{2+}; 0,03 g Ce^{3+}; 0,034 g Tb^{3+}
* calculated from the experimental amount of phosphor and residual solutions obtained

The content in the residual metals, in the matured solutions and in the washing solutions decreases with increasing of pH. It is observed that in the matured solutions Ca remains unreacted in the proportion of 53,5% (pH 7), 34,7% (pH 9) şi 4,8% (pH free). In the

solution obtained at pH 11 Ca was not identified. Washing solutions I and II of the pH 11 sample contain traces of Ca, as a result of its redissolution from the precipitate. Unreacted Y was found in smaller proportions (between 0,01% and 0,13%) in the maturation solutions. This is explained by the large difference between the solubility products of calcium hydroxides and yttrium that form during precipitation. ($K_{Ca(OH)2} = 5 \cdot 10^{-6}$; $K_{Y(OH)3} = 1 \cdot 10^{-22}$) [25]. Ce and Tb were identified only as traces in the residual solutions. The amounts of metals identified in the phosphors show that the sample synthesized at pH 11 has the closest composition to the theoretical one. The total cations experimentally identified is slightly lower than the theoretical values due to losses during the washing stages.

5.4.3 Structural and morphological characterization of samples

For a better understanding of the precipitation processes, precursors with or without TEOS addition, were structurally investigated. In Figure 1 are shown the FTIR spectra and XRD patterns of precursors prepared at different pH, before addition of TEOS. All precursors present a wide absorption band in the range of 3450 cm^{-1} corresponding to the hydroxyl stretching (–O–H) due to the water crystallization [28].
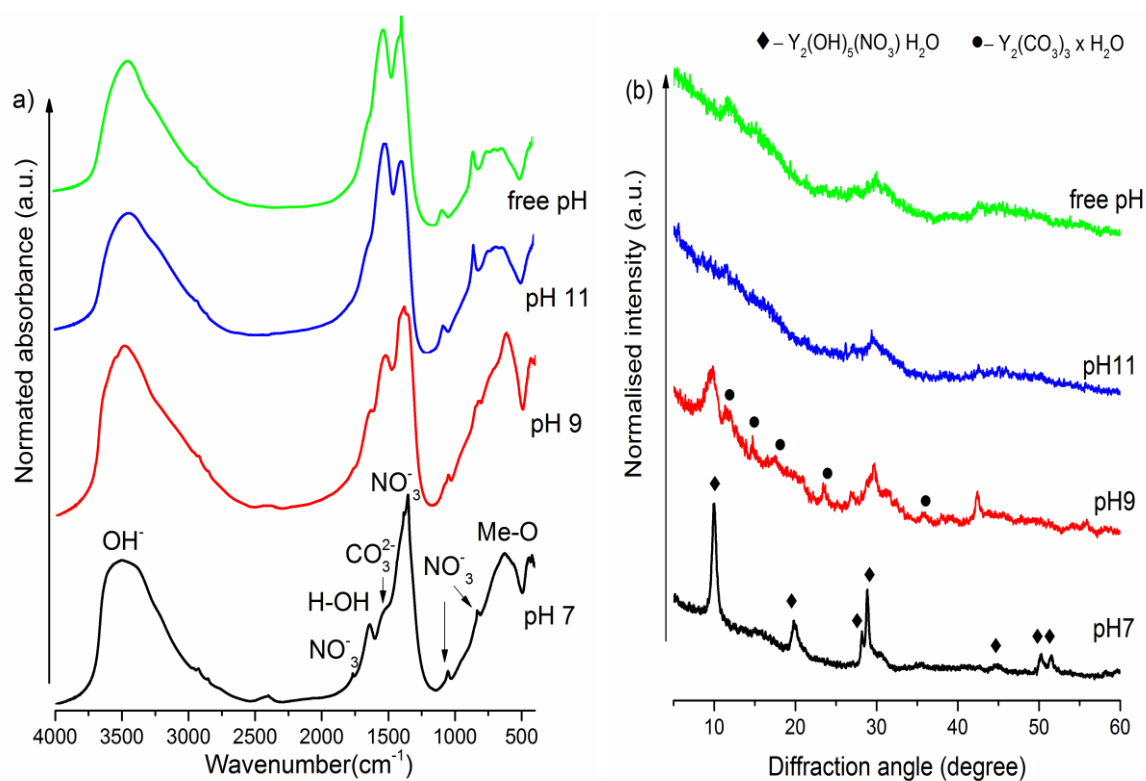
Figure 5.22. FTIR spectra (a) and XRD patterns (b) of precursors before addition of TEOS

Moreover, the deformation vibrations of water molecules (H-O- H) are represented by peaks in the region of 1637 cm^{-1} [33,34]. Bands at 1767 cm^{-1}, 1385 cm^{-1} and 856 cm^{-1} are associated with the vibrations in NO_3^- group [33], while vibrations under 650 cm^{-1} are due to M-O vibration (M= Y, Ca, Ce, Tb). At pH7, an absorption band as a shoulder is observed at 1520 cm^{-1} assigned to vibrations of carboxylate group, which may originate from CO_2 absorption when precursor is exposed to air [34,35]. However, according to the spectra shown in Figure 1, the band at 1520 cm^{-1} becomes more and more structured as the pH increase from 7 to 11, indicating the formation of carbonate compounds [33].

Based on FT-IR spectra, we can say that the precursors have a complex composition containing nitrates, hydroxides and carbonates groups in varying proportions. XRD diffraction patterns shown in Figure 5.22.b, shows that the structures of the precursors consist of amorphous and crystalline phase. The crystalline phase was identified as $Y_2(OH)_{5,14}(NO_3)_{0,86}.H_2O$ (PDF 321435). At pH 9 new diffraction lines appear belonging to $Y_2(CO_3)_3.H_2O$ (PDF 471828). No calcium compounds and silicon compounds were identified. The degree of crystallinity was evaluated as the ratio between the area of the diffraction peaks in the crystalline phase and the total diffraction surface, which sums up both the crystalline peaks and the amorphous phase, using the Reflex program in the *Material Suite Software* [36]. The crystallite size was obtained from the bandwidth at half the intensity of the maximum diffraction line, using the Scherer equation (5.13). Crystallite size decreases with increasing pH from 14,6 nm (pH 7) to 4,5 nm (free pH). The diffraction lines for pH 9 and pH 11 are very noisy and small to obtain exact crystallite size values. The values obtained of 6,2 nm (pH 9) and 4,7 nm (pH 11) are useful for information purposes only. The degree of crystallinity of the samples decreases with increasing pH as follows: 36% (pH 7), 25% (pH 9), 6% (pH 11), 5% (free pH). To obtain adequate structural information on the formation of the crystalline structure of apatite, it is necessary to correlate the FT-IR spectra with the XRD patterns of apatites obtained under stoichiometric and non-stoichiometric conditions at different pH, shown in Figure 5.23 [28]. The FT-IR spectra (Figure 5.23.a, c) of the sample prepared at pH 7 reveal the presence of a well-defined band at 560 cm^{-1} due to the vibration of the Y-O bonds in the Y_2O_3 phase [34] and several other smaller bands located at 1041 cm^{-1}, 1024 cm^{-1}, 938 cm^{-1}, 880 cm^{-1} and 868 cm^{-1} attributed to the vibrations of the Si-O-Si bonds in the Y_2SiO_5 phase [34]. The results obtained are in concordance with XRD measurements. At pH 9, the vibration bands in the 800-1100 cm^{-1} range become better

defined indicating rearrangements of the atoms in the crystal lattice as a result of the formation of the hexagonal phase of apatite along with the Y_2SiO_5 and Y_2O_3 phases.
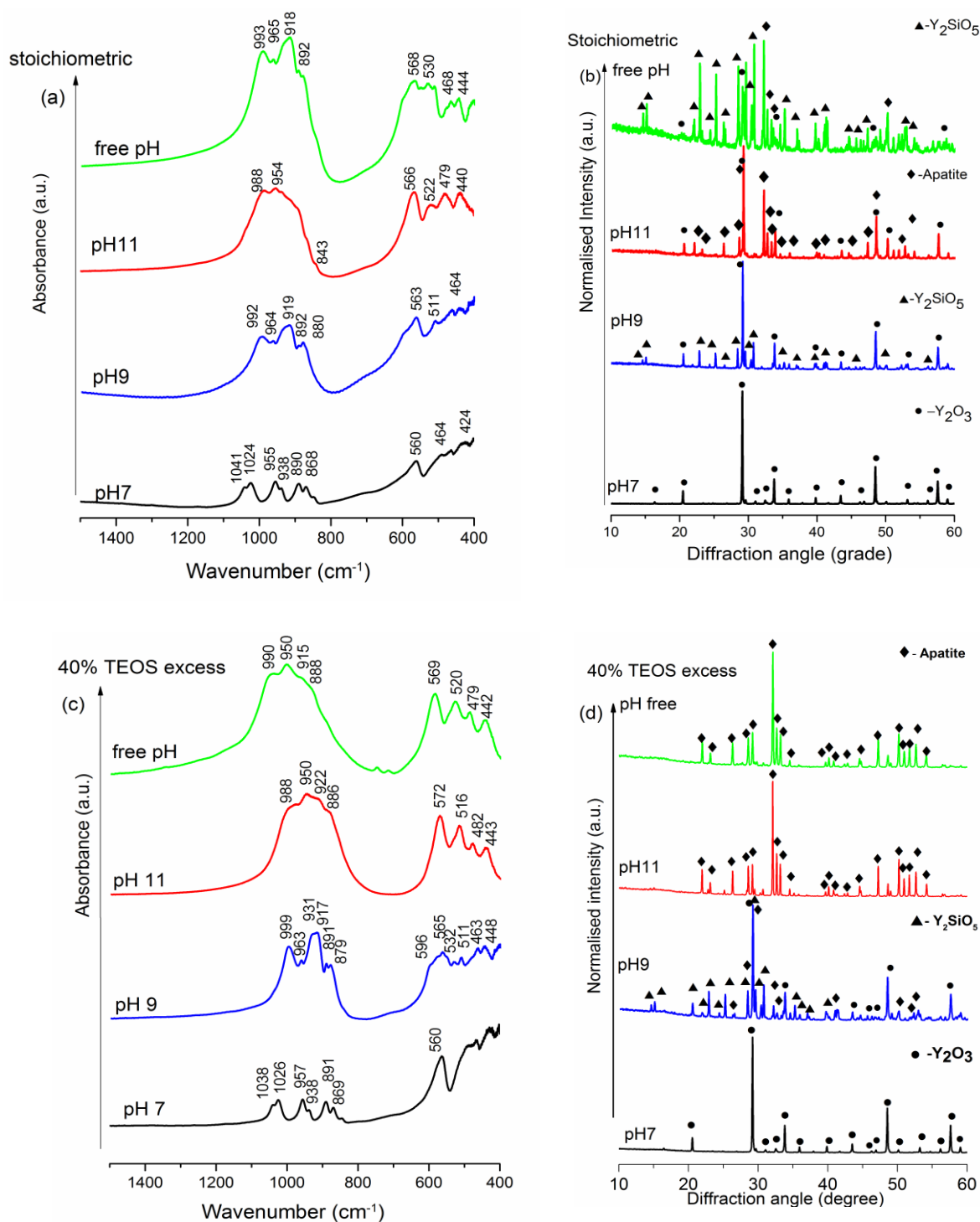
Figure 5.23. FTIR spectra (a, c) and XRD patterns (b, d) of samples prepared in stoechiometric conditions and with 40% excess of TEOS at different pH

The effect of the TEOS addition on the apatite phase purity is more evident for samples prepared in alkaline medium (pH 11, free pH), as can be seen from Figure 5.23.b, d. The FT-IR spectra of the pH 11 and free pH samples differ substantially from those of the pH 7 and pH 9 samples. Well defined bands located at ~900 cm^{-1}, 950 cm^{-1}, 915 cm^{-1}, 880 cm^{-1}, are assigned to asymmetric stretching vibration of Si-O-Si bonds in the apatite phase [14]. Bending vibrations of Si-O-Si bonds in the domain 400÷570 cm^{-1}, visible as four well-defined bands, slightly decreasing in intensity, are the specific pattern of apatite formation [14].

The pH during precipitation plays a decisive role in achieving the pure apatite phase. We found that regardless the stoichiometry, at pH7, cubic yttrium oxide (PDF 83-0927) is the majority phase (98%) and Y_2SiO_5 (PDF 52-1810) is minority phase (2%) (PDF 521810). Sample prepared at pH 9, in stoichiometric conditions, contains 27% Y_2O_3 and 73% Y_2SiO_5 (PDF 742158).

When 40% excess of TEOS is used, the apparition of 2% of apatite phase (PDF 30-1457) is observed along with Y_2O_3 and Y_2SiO_5. The phase analysis was performed using the reference intensity ratio (RIR) method [37]. An interesting observation is the modification of the Y_2SiO_5 space group with the increase of pH. Sample prepared at pH 7, contains monoclinic Y_2SiO_5 belonging to P21/c space group (a = 9,014 Å, b = 6,926 Å, c = 6,64 Å, β = 106,68^o) while sample prepared at pH 9 contains monoclinic Y_2SiO_5 belonging Ic /c space group (a = 9,014 Å, b = 6,72 Å, c = 12,49 Å, β = 102,6^o). The space group of cubic Y_2O_3, remains unchanged (Ia-3, a = 10,09 Å) for both pH 7 and pH 9. No other phases such as SiO_2, CaO, $Y_2Si_2O_7$ were identified. The main compound identified in stoichiometric samples prepared at pH11 and free pH was $Y_{4,67}(SiO_4)_3O$ (PDF30-1457) belonging to the hexagonal system with lattice parameters of a = 9,347 Å and b = 6,727 Å. This compound is equivalent with $Y_{9,34}(SiO_4)_6O_2$. Pure apatite was obtained in case of samples prepared at pH 11 and free pH when 40 % excess TEOS is used (fig 4c). In the supplementary material, the XRD patterns reveals that the excess of 40% TEOS represents an optimal value to obtain pure apatite while lower and higher values (35%, 45%) of TEOS does not assure disappearance of Y_2O_3 and Y_2SiO_5 phases. The crystalline mean size (D_{eff}) and root mean square (rms) of the microstrains $< \varepsilon^2 >^{1/2}$ were evaluated using Powder Cell computing program [38] and Williams Hall plot [24]. Phase analysis, crystallite size and strain of phosphor samples are given in table 5.6 [29].

Table 5.6. Phase analysis, crystallite size and strain of samples prepared with 40% excess of TEOS at different pH

Sample	pH 7	pH 9	pH 11	free pH
Phase composition	Y_2O_3*/Y_2SiO_5	Y_2O_3*/Y_2SiO_5/apatite	apatite	apatite
D_{eff}	105,6	77,0	66,5	92,9
ε (%) 10^{-4}	4,2	5,2	8,1	3,5

main phase

It is worth mentioning that the crystallite sizes and lattice strains are varies in the samples pH 11 and free pH which both contain pure apatite phase. This demonstrates, once again, that the crystal structure is influenced by the pH during precipitation, with implications on the apatite luminescence, presented in Chapter 6.

The shape and particle size of apatite powders, obtained from precursors at different pH, are illustrated by SEM images presented in Figure 5.24 [28].
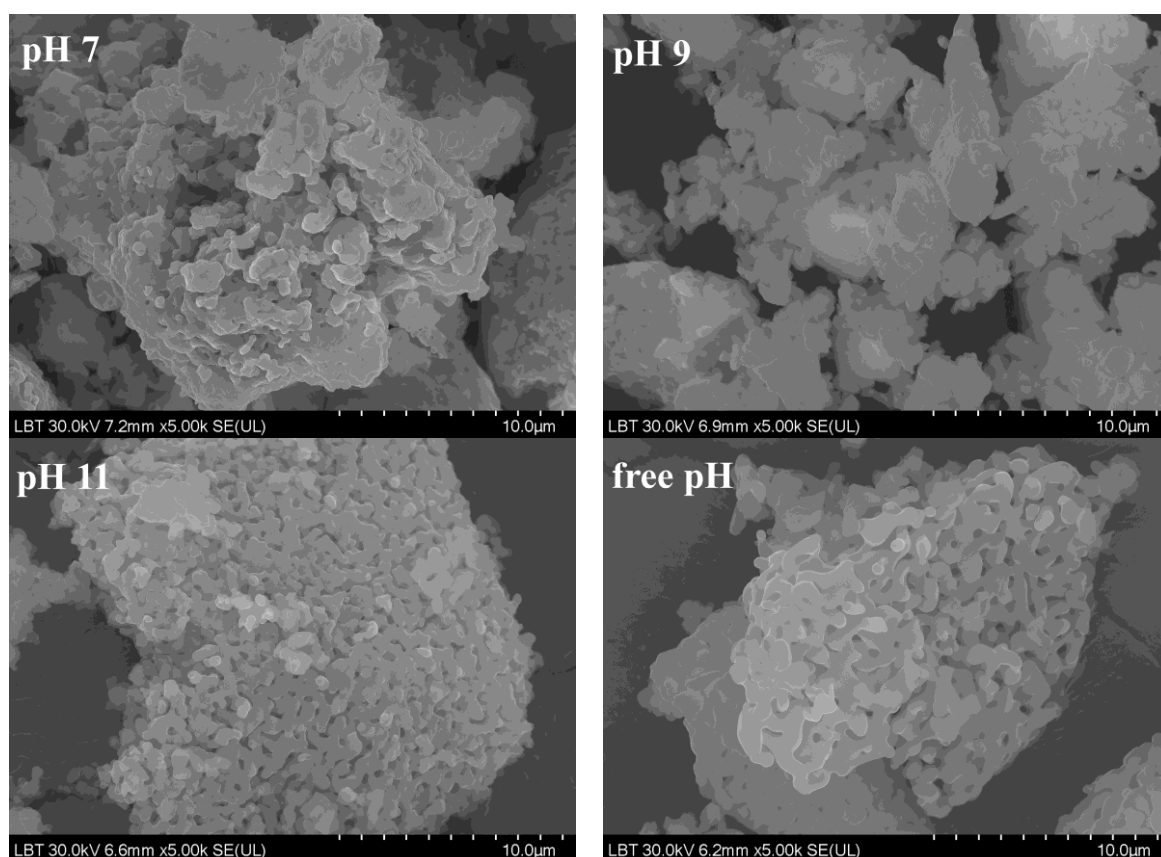
Figure 5.24. SEM images of samples prepared at pH 7; pH 9 ; pH11; free pH with 40% TEOS excess

Depending on the pH, the phosphors are constituted of submicron particles of different shapes, agglomerated in aggregates of ~20 μm. At lower pH (7 and 9) the particles have an irregular shape and size, while at higher pH (11 and free) the particles become rounded and homogeneous with a spongy appearance.

5.6 The host lattice and the activator in the *Combustion* method

Various apatite host lattice have been synthesized by the *Combustion* method. The influence of different cations on the formation of the apatite structure was studied. In this respect, trivalent ions of rare earths were used: La^{3+}, Y^{3+}, Ce^{3+}, Tb^{3+} and divalent alkaline earth metals ions (Ca^{2+}, Mg^{2+}), to generate compositions such as La^{3+}, Mg^{2+} -Y^{3+}, Ca^{2+} -Y^{3+}. As activators were used: Ce^{3+}, Tb^{3+}, Eu^{3+} and Bi^{3+}. The preparative conditions and apatite series prepared by Combustion are reunited in Table 5.10.

Table 5.10. Experimental parameters of luminescent apatites obtained by *Combustion*

Host lattice	Activator		Thermal treatment		Theoretical formula of final compound
	Cations	Concentration (%) *	(°C)	(h)	
Different host lattices and activators					
$La_{10}(SiO_4)_6O_3$	Bi^{3+}	1,5	1200	4	$La_{9,85}Bi_{0,15}(SiO_4)_6O_3$
$Y_{10}(SiO_4)_6O_3$		1,5			$Y_{9,85}Bi_{0,15}(SiO_4)_6O_3$
$Mg_2Y_8(SiO_4)_6O_2$		1,0			$Mg_2Y_{7,92}Bi_{0,08}(SiO_4)_6O_2$
$Ca_2Y_8(SiO_4)_6O_2$		1,0			$Ca_2Y_{7,92}Bi_{0,08}(SiO_4)_6O_2$
$Ca_2Y_8(SiO_4)_6O_2$	Ce^{3+}	1,5	1400	4	$Ca_2Y_{7,85}Ce_{0,12}(SiO_4)_6O_2$
	Tb^{3+}	1,5			$Ca_2Y_{7,85}Tb_{0,12}(SiO_4)_6O_2$
	Eu^{3+}	1,5			$Ca_2Y_{7,85}Eu_{0,12}(SiO_4)_6O_2$
	Ce -Tb	1,5 - 1,5			$Ca_2Y_{7,76}Ce_{0,12}Tb_{0,12}(SiO_4)_6O_2$**[1]**
	Ce -Tb-Eu	1,5- 1,5 - 1,5			$Ca_2Y_{7,64}Ce_{0,12}Tb_{0,12}Eu_{0,12}(SiO_4)_6O_2$

[1]*sample also prepared by the S-G method*

Host lattice	Activator		Thermal treatment		Theoretical formula of final compound
Activator concentration					
$La_{10}(SiO_4)_6O_3$	Bi^{3+}	0,25	1200	4	$La_{9,975}Bi_{0,025}(SiO_4)_6O_3$
		0,50			$La_{9,95}Bi_{0,05}(SiO_4)_6O_3$
		1,00			$La_{9,90}Bi_{0,10}(SiO_4)_6O_3$
		1,50			$La_{9,85}Bi_{0,15}(SiO_4)_6O_3$
		2,00			$La_{9,80}Bi_{0,20}(SiO_4)_6O_3$
		3,00			$La_{9,70}Bi_{0,30}(SiO_4)_6O_3$

* *reported at RE (RE^{3+} = La, Y)*

5.6.1 Thermal behavoiur of precursor

Since the thermal behavior of the precursors is similar, the thermal behavior of lanthanum silicate gel (LSO) is shown in Figure 5.29.a by the TG and DTA curves. The decomposition of the gel, with a total mass loss of 75,7%, takes place in five stages well highlighted on the TG curve, with significant mass losses ending at 600^oC. The value of the theoretical mass loss, calculated based on stoichiometric reaction is 76,5%, close to the experimental value. Using aspartic acid as a fuel, the theoretical combustion decomposition of lanthanum silicate gel is as follows:

$$10La(NO_3)_3 + 10C_4H_7NO_4 + 6SiC_8H_{20}O_4 + 72O_2 + H_2O \rightarrow$$
$$La_{10}(SiO_4)_6O_3 + 88CO_2\uparrow + 96H_2O\uparrow + 20N_2\uparrow \qquad 5.14$$
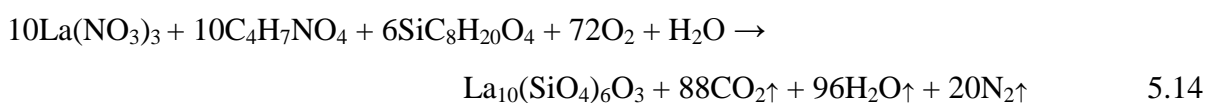
The decomposition processes can be more rigorously attributed if they are correlated with the gases released during the heating process.

Figure 5.29.b shows the DTG curve of the gel-precursor, which is well correlated with the Gram-Schmidt diagram of the gases released during the heat treatment (c).
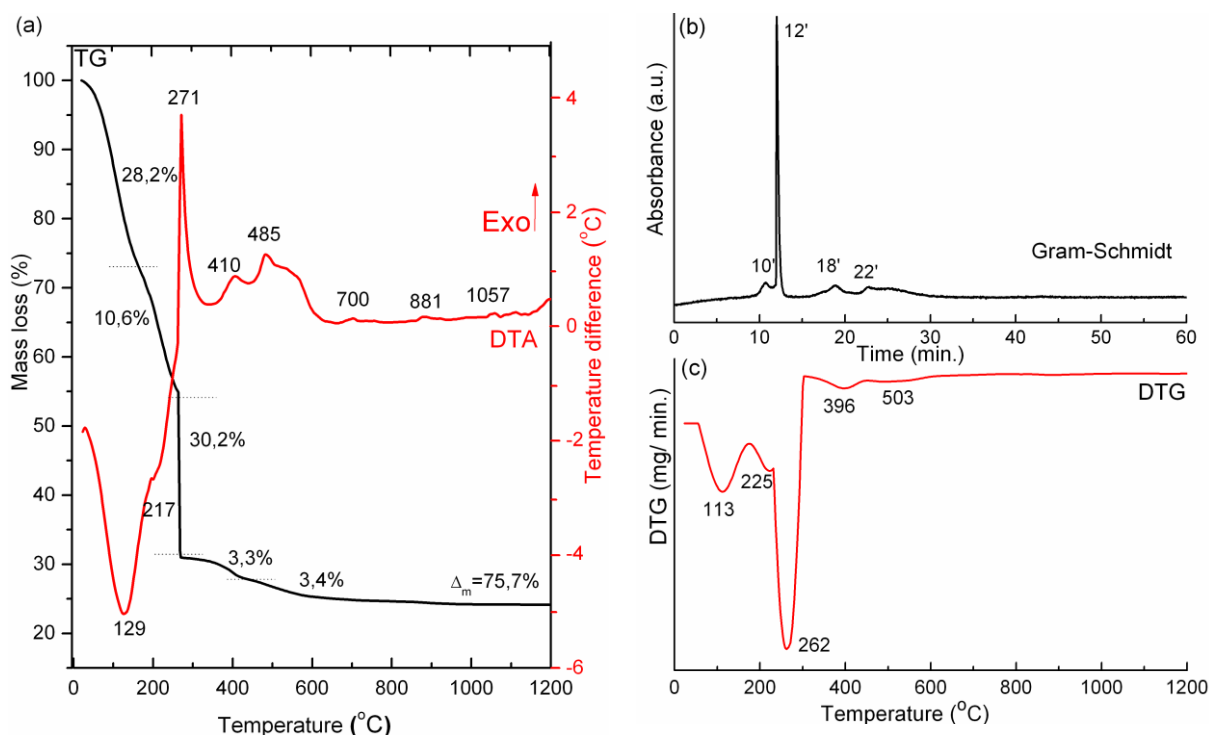
Figure 5.29. TG, DTA curves (a), Gram-Schmidt diagram (b) and DTG curve (c)

Gram-Schmidt diagram in Figure 5.29.b provides an overview of the entire LSO decomposition process, showing that the largest gas release occurs at minute 12, accompanied by a major mass loss, as shown in from the TG curve.

In the first stage of decomposition, an endothermic process is observed on the DTA curve (Figure 5.29.a), having a maximum at 129^oC, which is associated with the loss of 28,2% water (21,5% theoretically). Moisture is removed in the first 5 minutes of heating. The dehydration process is closely followed by another decomposition step, which takes place between 168^oC and 250^oC, with a mass loss of 10,6%, marked by a small endothermic effect at 217^oC. At 230^oC aspartic acid can release H_2O by condensing into polyaspartic acid [40,41]. Lanthanum nitrate can decompose into intermediate compounds such as: $La(OH)_2NO_3$ or $LaONO_3$ [42]. The mass loss of this stage (10,6%) is lower than the theoretical value of the reaction mentioned above, the explanation being that the decomposition initiated at 217^oC, does not have enough time to occur, because it is taken over by spontaneous combustion from 262^oC (Figure 5.29.c), accompanied by a strong exothermic effect, marked at 271^oC on the DTA curve (Figure 5.29). The reaction between nitrates and aspartic acid begins at minute 11 with a massive release of CO_2 along with nitrogen oxides (NO_2, N_2O) being confirmed by the Gram-Schmidt diagram (Figure 5.29.b). The process is highlighted as an abrupt decomposition step with a loss of 30,2%, accompanied by a strong exothermic reaction with a maximum at 271^oC on the DTA curve. Over 300^oC, small losses of CO_2 (3,3% and 3,4%) are detected, suggesting the presence of organic residues or species of lanthanum carbonate ($La_2O_2CO_3$) [43] that may result after combustion. The two small exothermic effects at 410^oC and 485^oC are due to oxidation processes. No more mass loss occurs above 600^oC. At 700^oC the amorphous phase of apatite is formed, followed by crystallization at 881^oC and phase transitions at 1057^oC, processes marked by slight exothermic effects on the DTA curve (Figure 5.29.a).

5.6.2 Structural characterization of samples

The structure and morphology of precursors and apatites obtained by combustion was highlighted by FT-IR and XRD spectroscopy.

The FT-IR spectra of precursors and apatites prepared with different cations are shown in Figure 5.31.

All gel precursors have a wide band in the range of wave numbers $3000 \div 3600$ cm^{-1}, characteristic of the stretching vibrations of O-H bonds in water and bands specific to NO^{3-}

groups, located at 1384 cm^{-1} and 1331 cm^{-1}, derived from $\nu(NO_2)$ in metalic nitrates [11]. The bands from ~1638 cm^{-1} coresponds to bending vibrations of the H-O-H bonds [11-13]. In the gels that contain Ca^{2+}, small additional bands appear at ~1100 cm^{-1}, 971 cm^{-1} from Si-O bonds in TEOS and other at 1204 cm^{-1}, specific to the vibration of C-O bonds in the CO_3^{2-} group, as following a possible carbonation of calcium nitrate [44].

As a result of the combustion process the ashes contain bands located at ~ 3405 cm^{-1}, 1638 cm^{-1}, wich decrease in intensity due to the moisture loss. A new band appears at ~1540 cm^{-1}, specific to asymmetric vibration ν_{as}C-O, both as a result of a possible adsorption of CO_2, from atmospheric humidity, and the formation of carbonated compounds such as lanthanum, yttrium, calcium oxy-carbonates ($La_2O_2CO_3$, $Y_2O_2CO_3$, $Ca_3O_2CO_3$). In addition, the band from ~ 960 cm^{-1} specific to Si-O-Si bonds appears, indicating the rearrangement of silicon in the SiO_4 network, still incompletely crystallized as apatite. The 500 cm^{-1} band, specific to Me-O-H bonds bending vibration is intensified indicating the presence of metal hydroxides [14], confirmed by EGA.
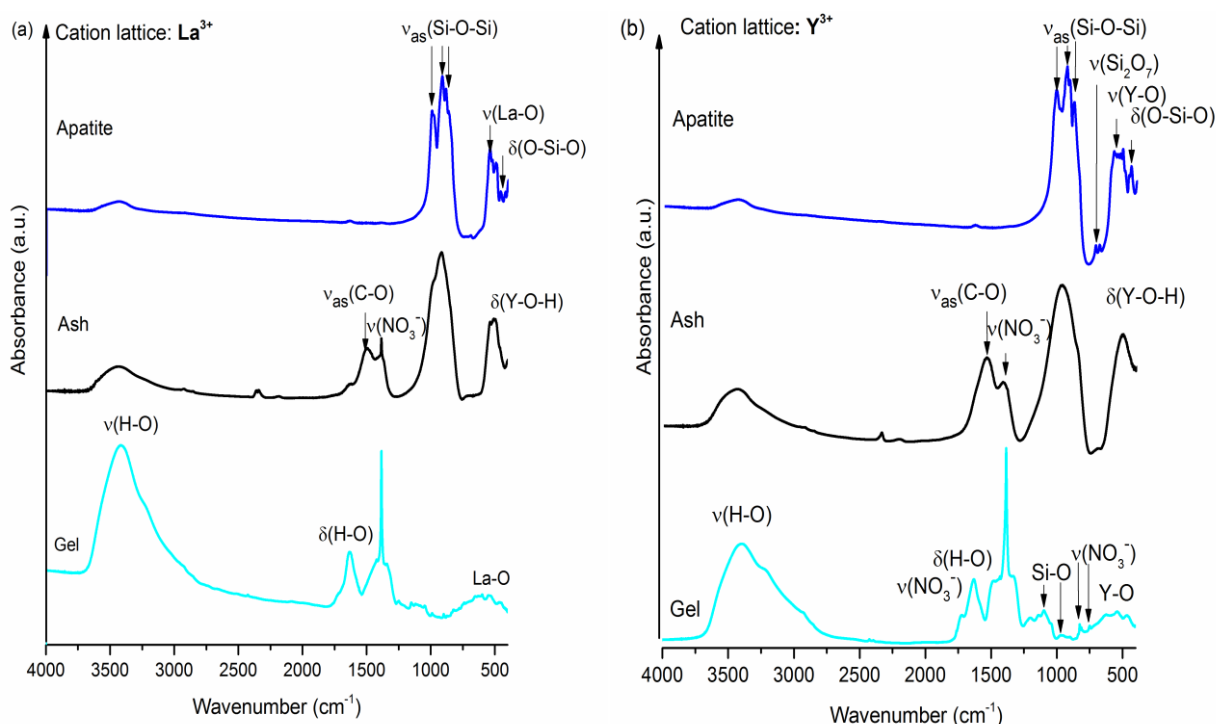
Figure 5.31. FT-IR spectrum of samples with La^{3+} (a), Y^{3+} (b) in the host lattice, for: gel - before combustion, ash - after combustion and apatite - after calcination

The heat treatment of the ashes leads to the almost complete disappearance of the vibrations in the range 1300÷1700 cm^{-1}, while new bands appear located at ~ 980 cm^{-1}, ~ 950 cm^{-1}, ~ 895 cm^{-1} due to the formation of the silicate lattice with apatite structure. Below 600 cm^{-1} there are 4 specific bands located at ~ 565 cm^{-1}, ~ 518 cm^{-1}, ~ 480 cm^{-1}, ~ 439 cm^{-1}, attributed to the vibrations of the Me-O and O-Si-O connections in the apatite lattice [14].

Apatite powder with Y content, has small additional bands located at 690 cm^{-1} and 720 cm^{-1}, attributed to the vibration of the Si-O bonds in the Si_2O_7 groups belonging to $Y_2Si_2O_7$, formed as a secondary crystalline phase that contaminate the apatite lattice [7].

The crystalline structure of the powders investigated by X-ray diffraction analysis are shown in Figure 5.32.
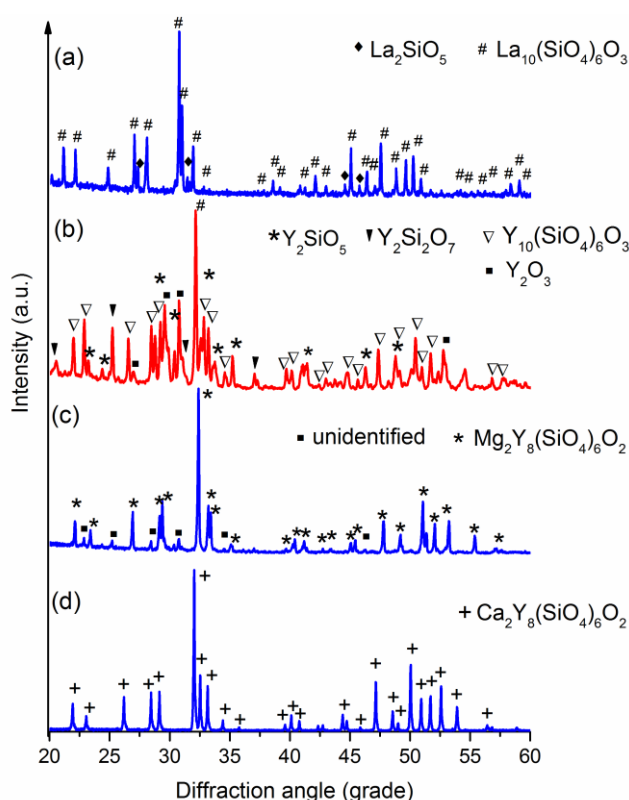
Figure 5.32. XRD patterns of apatite powders $La_{10}(SiO_4)_6O_3$ (a),

$Y_{10}(SiO_4)_6O_3$ (b), $Mg_2Y_8(SiO_4)_6O_2$ (c), $Ca_2Y_8(SiO_4)_6O_2$ (d)

The powder based on La contain a major phase of apatite crystallized in hexagonal system with spatial group P6$_3$/m, according to PDF 530291. The main line of the hexagonal structure of $La_{10}(SiO_4)_6O_3$ is centered at a diffraction angle 2θ = 30,7^o. The powder also has some very small additional diffraction lines, located at 20,1^o; 27,2^o; 31,4^o; 44,5^o; 48,4^o; 54,1^o,

attributed to secondary phase as traces of monoclinic La_2SiO_5 corresponding to PDF 400234 (Figure 5.32).

The Y- powder contain apatite phase according to PDF 301457 and secondary phases of hexagonal Y_2O_3 (PDF 201412), monoclinic Y_2SiO_5 (PDF 410004) and $Y_2Si_2O_7$ as traces (PDF 742163). The main line of the hexagonal apatite structure is centered at $2\theta = 32^o$ diffraction angle. Additional lines of lower intensity, located at 27°; $29,6^o$; $30,7^o$; $40,1^o$; $52,9^o$ are atributed to Y_2O_3, those located at $29,1^o$; $29,5^o$; $30,7^o$; $32,5^o$; $33,7^o$; $46,2^o$; $48,1^o$ are atributed to Y_2SiO_5 and those located at $25,5^o$; $31,3^o$; $33,4^o$; 37° belong to $Y_2Si_2O_7$ phase.

Substitution of Y^{3+} with Mg^{2+} ions in the host lattice leads to an almost structurally pure apatite, with the formula $MgY_4(SiO_4)_3O$ according to PDF 201410, isostructural with $Mg_2Y_8(SiO_4)_6O_2$, having the main diffraction line centered at a diffraction angle of $2\theta = 32,3^o$.

Substitution of Mg^{2+} with Ca^{2+} ions, ensures the formation of a pure apatite structure containing hexagonal phase type $Ca_4Y_6(SiO_4)_6O_2$ (PDF 270093), isostructural with $Ca_2Y_8(SiO_4)_6O_2$.

Performing XRD analysis, the microstructural parameters of the apatite samples obtained by *Combustion* are sumarised in Table 5.11.

Table 5.11. Microstructural parameters of apatites obtained by *Combustion*

Apatite code	Cell parameters		
	$a = b$ (Å)	c (Å)	V ($Å^3$)
LaAp	9,723	7,187	588,497
YAp	9,350	6,731	513,651
MgYAp	9,298	6,635	496,763
CaYAp	9,352	6,796	514,775

The differences between the microstructural parameters of the apatite lattice are given by the ionic radii of cations: ($r_{La(I)} = 1,1$ Å, $r_{La(II)} = 1,216$ Å; $r_{Y(I)} = 0,96$ Å, $r_{Y(II)} = 1,075$ Å; $r_{Mg(I)} = 0,72$ Å, $r_{Mg(II)}$ $0,89$ Å; $r_{Ca(I)} = 1,06$ Å, $r_{Ca(II)} = 1,18$ Å) [45]. Thus, the elementary cell with the highest volume belongs to LaAp and the smallest structural dimensions belong to the apatite constituted by the cation pair Mg^{2+} -Y^{3+}.

6. LUMINESCENT PROPERTIES OF SILICATES WITH APATITE STRUCTURE

Compounds belonging to the structural family of apatites, with chemical formula $M_{10}(TO_4)_6X_2$ (M = Ca^{2+}, Sr^{2+}, La^{3+}, Y^{3+}, etc., T = Si^{4+}, P^{4+}, S^{4+} şi X = O^{2-}, Cl^-, F^-) and spatial group $P6_3/m$, are attracting more and more attention in recent years as host lattice for lanthanide ions, being used in laser applications and as luminescent materials [1-5]. Apatites presents two cationic sites with different symmetries: C_3 (4f) - CN9; Cs (6h) - CN7. Preferential incorporation of rare earth activator ions and transition metals may influence the luminescence of apatites [6].

The studies on the luminescent properties of apatites were focused on obtaining new phosphors with applications in the field of efficient lighting systems.

6.1 The influence of some experimental parameters on the luminescence of apatites $A_xRE_{10-x}(SiO_4)_6O_{3-x/2}$

In the process of phosphor development, a number of experimental parameters must be taken into account, which must be chosen to contribute to the best performance of the material. Ropp makes a classification of parameters, which can be of two types: dependent and independent [7]. The parameters that affect the luminescence are: ►the type of activator; ►the activator concentration; ►nature of the host lattice; ►synthesis method; ►calcination temperature; ►calcination time; ► reactants ratio

6.1.1 Nature and concentration of activator

The effect of single and multiple doping with rare earth ions (RE^{3+} = Ce, Tb, Eu) on the luminescent emission of calcium-yttrium silicate, described by the formula Ca_2Y_8 $(SiO_4)_6O_2$ (noted CYSO), obtained by Combustion, is discussed. The conditions for the synthesis of the samples are presented in section 5.6. Figure 6.1 shows the emission and excitation spectra of CYSO apatite doped with different RE ions and the energy transfer diagrams of the activating ions.

By excitation of the CYSO: Ce with UV radiation in the cerium band (λem = 406 nm) the electrons jump occurs in Ce^{3+} ions ($4f^1$), from the fundamental level $4f$ to the upper level $5d$, which generates a wide excitation band with a maximum at 321 nm (Figure 6.1.a). The return of the electrons to the ground state takes place with a luminescent emission in the blue zone of the visible spectrum.
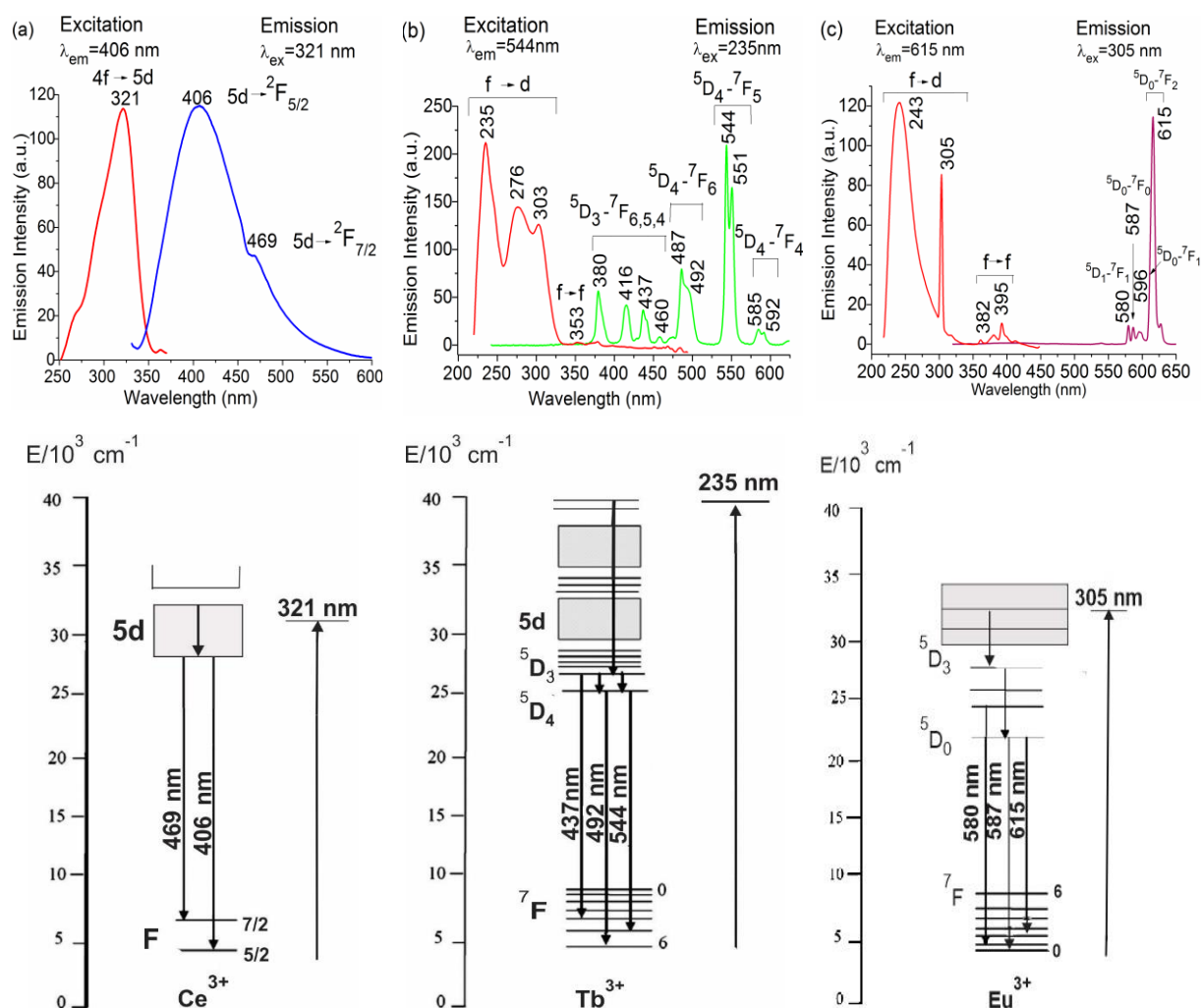
Figure 6.1. Excitation, emission spectra and energy diagrams corresponding to CYSO apatite doped with Ce^{3+}(a), Tb^{3+}(b) şi Eu^{3+}(c)

The emission spectra consist from an asymmetric band with maxima located at 406 nm and a shoulder at 469 nm, attributed to the transitions $5d \rightarrow {}^2F_{5/2}$, respectively $5d \rightarrow {}^2F_{7/2}$. Transitions specific to Tb^{3+} ($4f^8$), can be divided in two groups, corresponding to spin allowed transitions (SP), *f-d* type and spin forbiden (SI), *f-f* type [9]. Doping with Tb^{3+} determines the appearance in the excitation spectrum (Figure 6.1.b), of wide bands with high intensity, located at 235 nm, 276 nm, 303 nm, attributed to the electronic transitions *f-d* in Tb^{3+} ions and bands with low intensity, located in the range 350÷500 nm, due to transitions *f-f* [10]. The emission spectra recorded by excitation at 235 nm, consists of narrow lines, attributed to transitions: $^5D_3 \rightarrow {}^7F_{6,5,4}$ (380÷460 nm); $^5D_4 \rightarrow {}^7F_6$ (487 nm şi 492 nm); $^5D_4 \rightarrow {}^7F_5$ (544 nm şi 551 nm); $^5D_4 \rightarrow {}^7F_4$ (285 nm şi 592 nm) [11]. Emision spectra in the form of

narrow lines is due to small energy differences between the ^7F_J layers (ground level). The luminescent color of the sample in the green area is given by the emission line located at 544 nm.

Doping with Eu^{3+} ($4f^6$) of CYSO apatite leads to a luminescence in the red area of the visible spectrum. The excitation spectrum of the sample (Figure 6.1.c), $\lambda em = 615$ nm, consists of a wide, asymmetric band, with a maxima at 243 nm and a sharp band located at 305 nm, due to electronic transitions *f-d* in Eu^{3+} ions and small bands at 382 nm, 395 nm, attributed to spin forbidden transitions *f-f* . The emission spectrum, recorded at the excitation of the sample at 305 nm, has several narrow lines, located at 580 nm ($^5D_1 \rightarrow ^7F_1$), 587 nm ($^5D_0 \rightarrow ^7F_0$), 596 nm ($^5D_0 \rightarrow ^7F_1$) şi 615 nm ($^5D_0 \rightarrow ^7F_2$) [4].

A simple way to obtain a white LED is to prepare a multiple activated phosphor, which emits at wavelengths in the spectral ranges: red, blue, green [12]. By combining the three basic colors in certain proportions, an emission of white light can be obtained.

For this purpose, a triple doping was performed, with equal molar concentrations of 1,5% Ce^{3+}, Tb^{3+} and Eu^{3+} of CYSO apatite. Literature shows that Eu^{3+} in $Ca_2Y_8(SiO_4)_6O_2$ show a preference for A (I) sites, a position in which the luminescence due to the $^5D_0 \rightarrow ^7F_2$ transitions is more intense. [13]. The excitation and luminescent emission spectra of apatite triple doped with Ce-Tb-Eu are shown in Figure 6.2. The excitation spectra (Figure 6.2.a) show the behavior of the CYSO:Ce-Tb-Eu phosphor upon excitation in the emission bands specific to each activating ion. Thus, the excitation spectrum in the Ce^{3+} band shows maxima located at 321 nm and 364 nm, the spectrum recorded in the Tb^{3+} band presents maxima at 230 nm, 321 nm and 379 nm and the excitation spectrum in the Eu^{3+} band highlighted three maxima positioned at 264 nm, 306 nm and 395 nm. The emission of the apatite sample at different excitation wavelengths can be followed in Figure 6.2.b. High emission intensities in the green zone can be observed at the excitation of the sample with 230 nm, in the Tb^{3+} band and in the red zone by excitation with 306 nm, in the Eu^{3+} band.
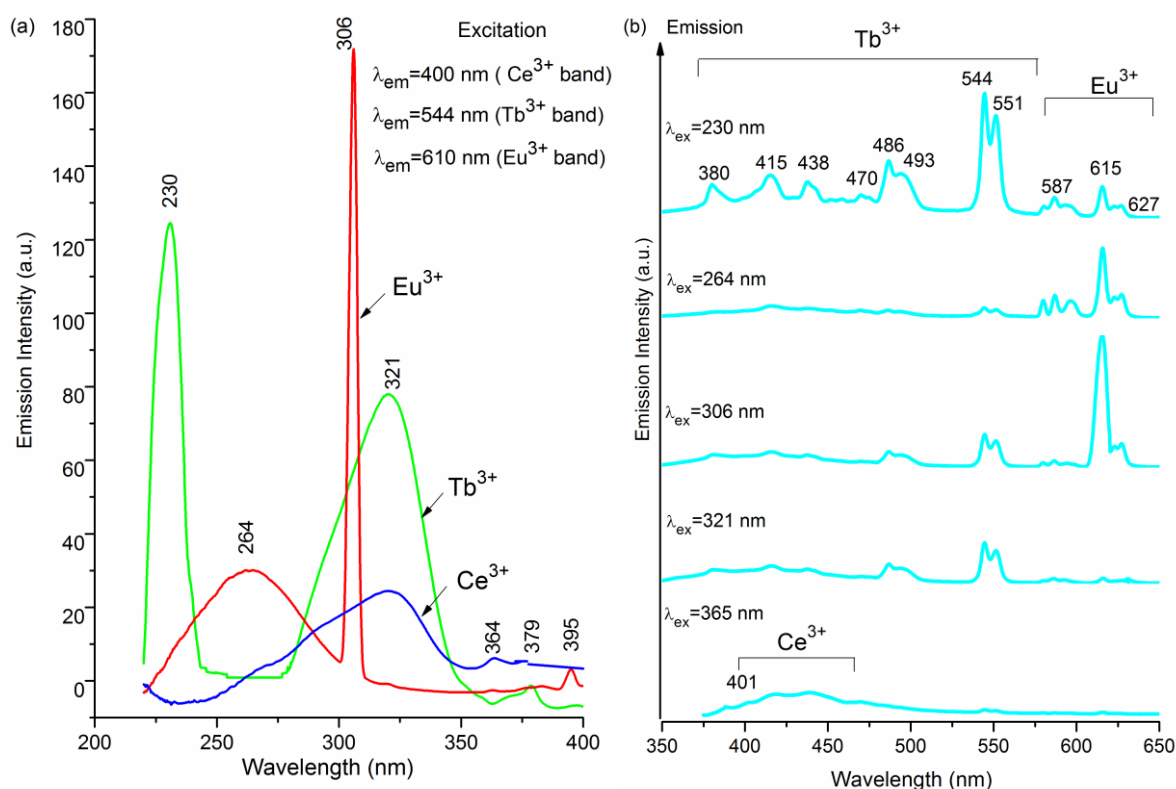
Figure 6.2. Excitation spectra (a) and emission at different excitation wavelengths (b)

of the CYSO phosphor: Ce-Tb-Eu

Excitation with 365 nm produces a white luminescence, with a predominant contribution of Ce^{3+}, which gives an application potential to the material in the manufacture of LEDs.

In Figure 6.3, the luminescent emission colors, under the UV lamp (365 nm), of the CYSO single doped and triple doped with Ce,Tb, Eu, can be observed.
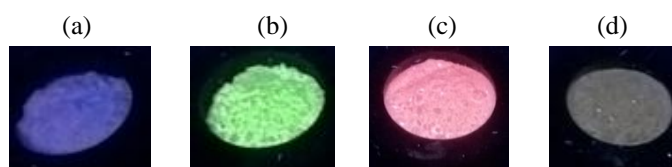
Figure 6.3. Emission color under the UV lamp (365 nm) of CYSO apatite

doped with Ce^{3+}(a), Tb^{3+}(b), Eu^{3+}(c), Ce^{3+} -Tb^{3+}-Eu^{3+}(d)

The influence of Ce^{3+} activator ion concentration on the luminescent emission of apatite $Ca_2Y_8(SiO_4)_6O_2$ was studied for samplee prepared by *Precipitation-mW*. 5 apatite-type samples doped with 0,5%; 1,5%; 3,0%; 6.0% and 9,0% Ce^{3+} concentrations were

synthesized. Ce^{3+} concentration (∗) was reported to 8 moles of Y. The calcination of the samples was done at $1400^{o}C$, 4h. In Figure 6.4, the emission spectra of CYSO:Ce apatites are presented under UV excitation radiation with different wavelengths. The spectra consist of wide asymetric bands, in the range 375÷475 nm, with maxima located at 400 nm in the blue zone of the visible spectrum. According to Blasse's theory, in the apatite lattice the cationic site (II), located near the interstitial oxygen, prefer to accommodate cations with high charge or low ionic radius to compensate the charge deficit [14].
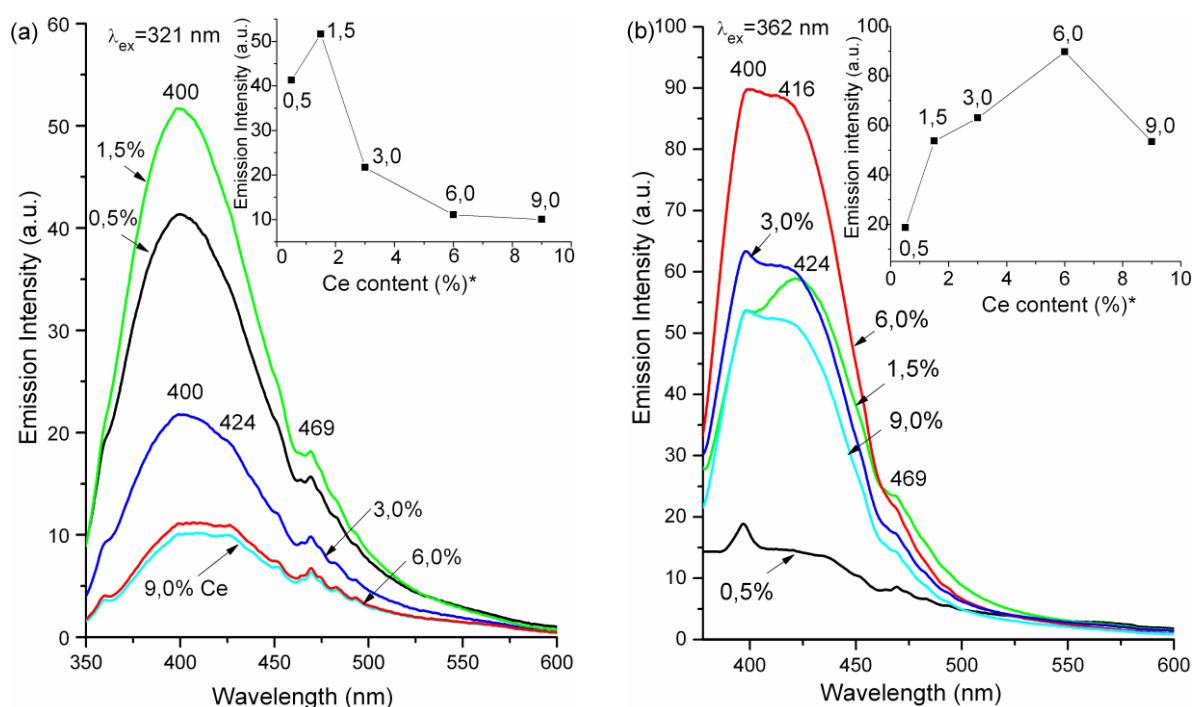
Figure 6.4. CYSO:Ce emission spectra at different excitation wavelengths

As a result, Ce^{3+} ions having a large radius (r = 1,196 Å, NC9), prefer to occupy site (I), with implications on the luminescent emission of the material. Under 321 nm excitation, the apatite doped with 0,5% Ce^{3+}, the emission maxima located at 400 nm and 469 nm (Figure 58 a) can be attributed to the electronic transitions of the Ce^{3+} (I) from the excited level 5d, on the two fundamental sublevels $^2F_{7/2}$ and $^2F_{5/2}$. At the doping level of apatite to 3,0% Ce^{3+}, the appearance of a small shoulder is observed, located at 424 nm, corresponding to the incorporation of Ce^{3+} ions also in position (II) [8]. Increasing doping level up to 9,0% Ce^{3+}, makes the shoulder at 424 nm more visible as a result of the incorporation of a larger part of the Ce^{3+} in position (II).

The emission intensity of the samples is influenced by both the concentration of the activating ion and the wavelength of the excitation radiation. Thus, by excitation with 321 nm the optimal concentration of Ce^{3+} in the phosphors with apatite structure proved to be 1,5% Ce^{3+} (Figure 6.4.a). It is observed that when the cerium content increases above this value, the emission intensity suddenly decreases due to the quenching luminescence. At 362 nm excitation, the maximum emission is reached at a higher doping level of 6,0% Ce^{3+} (Figure 6.4.b).

In order to replace rare earths with more accessible cations and to obtain a new type of phosphor with applicability in the field of LEDs, the doping of apatite-type silicates with Bi^{3+} ions was studied. This type of activator was used in many other host lattice according to literature data [15,16]. Bi^{3+} ions $(6s^2)$ generate luminescence in the host lattice through electronic transitions between the fundamental level $6s^2$ and excited 6s, 6p levels [17]. Through the transitions: $^1S_0 \rightarrow {}^3P_1$; $^1S_0 \rightarrow {}^1P_1$, Bi^{3+} ions generate wide absorption bands in the UV or nUV range. It should be mentioned that electronic transitions, type: $^1S_0 \rightarrow {}^3P_0$, $^1S_0 \rightarrow {}^3P_2$ are strictly forbidden by the selection rules Δj [18,19]. The luminescence of the $La_{10}(SiO_4)_6O_3$ apatite type was investigated, doping with different Bi^{3+} concentrations, as follows: 0,25%, 0,50%, 1,00%, 1,50%, 2,00%; 3,00%. The Bi^{3+} concentration was reported at 10 moles of La. In Figure 6.5, the excitation and luminescent emission spectra of apatites with variable Bi content are shown. The excitation spectra presented in Figure 6.5.a, consist of 2 wide bands, with maxima located at 227 nm and 301 nm. Bi^{3+} ions, substituting the La^{3+} cations of the apatite host lattice, can simultaneously occupy positions (I), NC9 and (II), NC7. The difference between the ionic radii of the two cations shows the preference of Bi^{3+} ions to accomodate in site (I). In this position, the Bi-O bonds are longer and weaker, therefore the excitation of Bi^{2+} cations requires lower energy (longer wavelengths). Thus, the excitation maxima from 227 nm and 301 nm, can be attributed to the $^1S_0 \rightarrow {}^3P_1$ transitions of Bi^{3+} ions located in positions La (II), respectively La (I), according to the data in the literature [20]. The emission spectra (Figure 6.5.b) consist of a wide, asymmetric band, with a maximum at 442 nm and a shoulder at 465 nm. The emission is due to the transitions $^3P_1 \rightarrow {}^1S_0$ in the Bi^{3+} (I), respectively Bi^{3+} (II). It is interesting to note that the ratio between the intensities of the two emission bands decreases with increasing activator concentration.
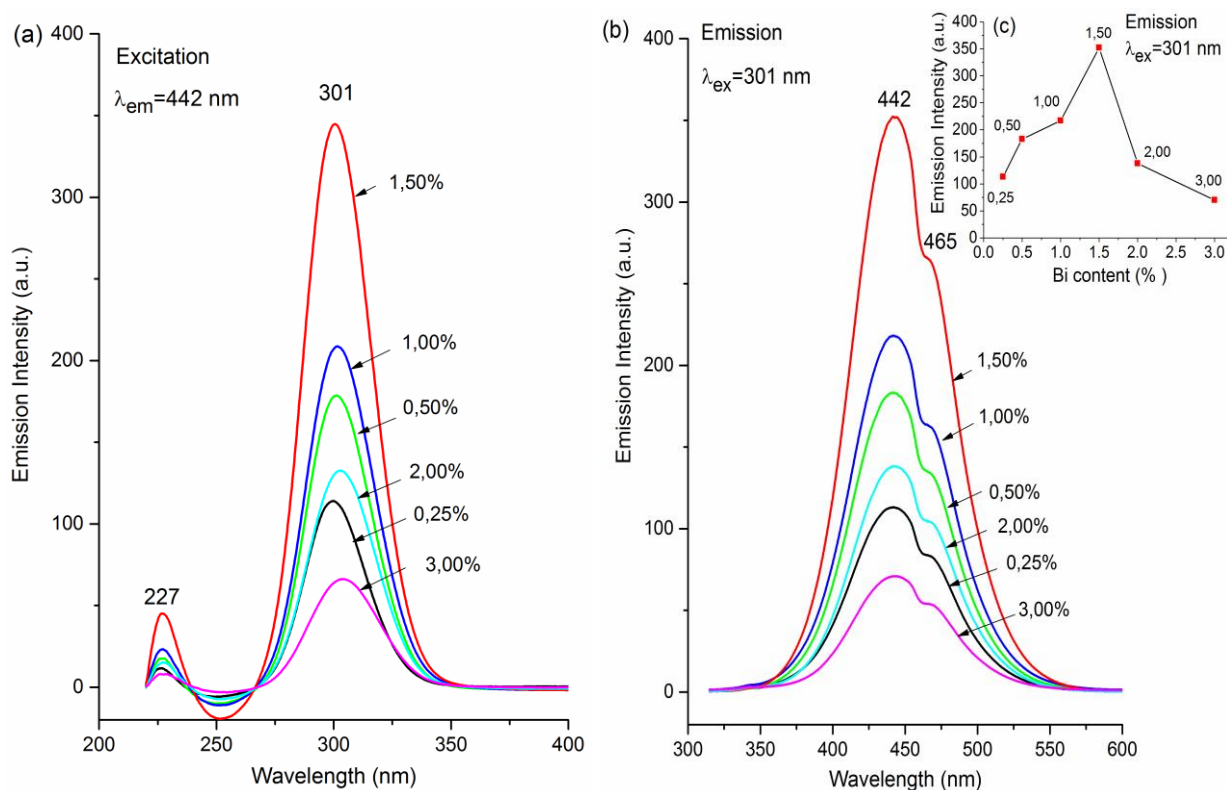
Figure 6.5. Excitation (a), emission spectra (b) and variation of emission intensity with Bi^{3+} content in $La_{10}(SiO_4)_6O_3$:Bi

This behavior suggests that at a higher activator concentration the number of doping cations incorporated at position II increases. Up to 1,5% Bi^{3+}, there is an increase in emission intensity followed by a dramatic reduction in luminescence above this value, as a result a *quenching of luminescence.* This phenomenon, which decreases the fluorescence intensity of a phosphor, can be caused by different processes such as: non-radiative energy transfer between the luminescent center and the host lattice and interactions betwin activator ions [7]. Due to the electronic configuration of the Bi^{3+} ($6s^2$), the optical properties of Bi phosphors are strongly influenced by the coordination number and the surrounding places in the lattice in which the activator is incorporated [21]. The luminescence produced by Bi^{3+} ions can be modulated from: UV, blue to green, depending on the symmetry of the host lattice, aspects that will be discussed in sub-chapter 6.1.2.

In conclusion, the luminescence color of apatites can be controlled by the appropriate choice of activator: red (Eu^{3+}), blue (Ce^{3+}, Bi^{3+}), green (Tb^{3+}) while the emission intensity is influenced by the activator concentration. For each activator it is necessary to determine the optimal concentration that produces maximum emission intensity.

6.1.5 pH during precipitation

The luminescence of $Ca_2Y_8(SiO_4)_6O_2:Ce^{3+},Tb^{3+}$ (CYSO:Ce,Tb) synthesized by precipitation at different pH, with molar excess of 40% TEOS was studied.

Figure 6.19 shows the excitation and emission spectra of apatites, which strongly depend on the pH during precipitation [32]. The broad aspect of the excitation spectra (Figure 6.19.a, b) suggests that the Ce^{3+} and Tb^{3+} form luminescent centers in different structural environment. As can be seen, the excitation spectra in the Ce^{3+} band (Figure 6.19.a) are dominated by bands located above 260 nm, while the excitation spectra in the Tb^{3+} band (Figure 6.19.b) are dominated by intense bands situated below 260 nm.

The samples obtained at pH 7 and pH 9 (Figure 6.19.a) shows a very low excitability, due to the fact that the samples are structurally impure, containing Y_2O_3 (pH 7) and Y_2SiO_5 (pH 9), confirmed by XRD (section 5.5). The sample obtained at pH 11, having a single apatite phase, shows a high degree of excitability in the range 260-380 nm, due to the electronic transitions of Ce^{3+} between the fundamental level $4f^1$ and 5d level. The small band at 243 nm is specific to transitions that occur in Tb^{3+} ions. Although the free pH sample is also structurally pure, the bands located at 298 nm, 320 nm are lower in intensity, while the 367 nm band is barely visible as a small shoulder. To assign these excitation bands we must take in consideration that apatites exhibits two nonequivalent crystallographic sites for Ca^{2+} and Y^{3+}, namely, M (I) site occupying the 4f position (C3 point symmetry) with nine-fold coordination and M (II) at the 6h position (Cs symmetry) with sevenfold coordination [33,34]. The M (I) sites are occupied disorderly by Y^{3+} and Ca^{2+}. On the other hand, the M (II) sites are occupied only by Y [33]. Based on this general remark, Ce^{3+} and Tb^{3+} can randomly substitute four cationic sites (Ca_I, Y_I, Ca_{II} and Y_{II}) characterized by symmetry groups C3 and Cs respectively. However, due to the close ionic radii of Ce^{3+} ($r_I = 1,196Å$, NC=9; $r_{II} = 1,07$ Å, N.C =7) and Tb^{3+} ($r_I = 1,095$ Å, NC=9; $r_{II} = 0,98$ Å, N.C =7) to Y^{3+} ($r_I = 1,075$ Å, NC=9; $r_{II} = 0,96$ Å, N.C =7), most probably the dopants will substitute Y^{3+} sites found in both C3 and Cs positions. Therefore, presence of multiple excitation bands (fig 7 a) can be attributed to the formation of Ce luminescent centres in M (I), M (II) sites same as due to the crystal field splitting of the excited 5d Ce configuration [35].
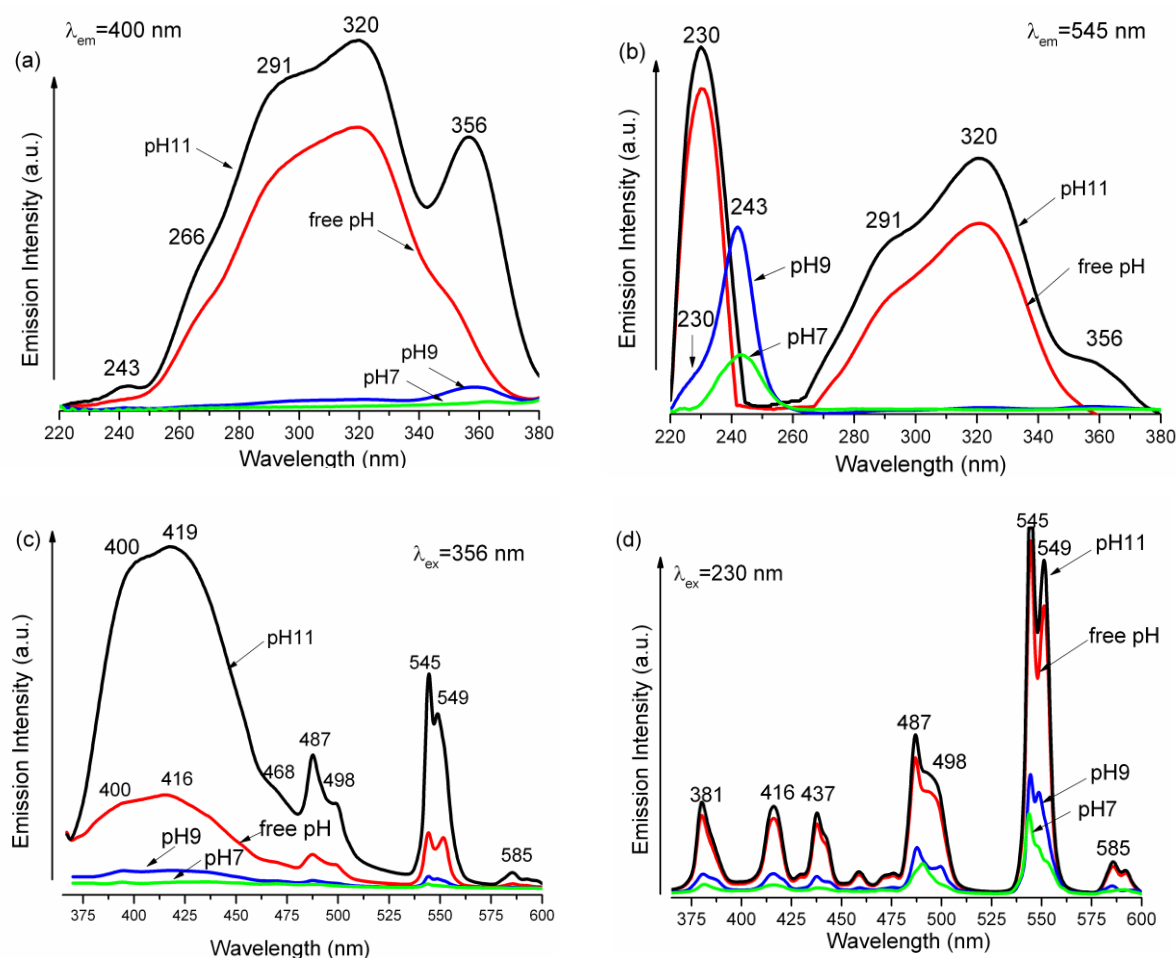
Figure 6.19. Excitation spectra in the Ce^{3+} (a) and Tb^{3+} bands (b) and coresponding emission spectra (c, d) of salmpes prepared at different pHs with 40% excess TEOS

The excitation spectra in Tb^{3+} band (fig 7b) of samples with pure apatite structure (pH11, free pH) reveals apparition of an intense band at 230 nm assigned to 4f^8 - 4f^{7}5d^1 transition in the Tb^{3+} ions [35,36] along with broad bands of Ce, while spectra for low purity phase samples (pH 7, pH 9) exhibits only a single band centered at 243 nm. Tb^{3+} incorporates in other host lattices than apatite, namely Y$_2$O$_3$ (pH 7 sample) or Y$_2$SiO$_5$ (pH 9 sample), which leads to different energy levels spitting shifting the excitation peak from 230 nm (pH11, free pH) to longer wavelengths (243 nm). The small excitation shoulder seen at 230 nm in sample pH 9 indicates the presence of small amount of apatite which is in concordance with XRD results (sub-chapter 5.5). Under excitation with 356 nm, the emission spectra (Fig 7c) show the asymmetric broad band of Ce^{3+} with two maxima situated at 400 nm and 419 nm that extend toward higher wavelength and followed by the well-defined bands of terbium in the range of 475-585 nm. Cerium emission consist of typical inter-configurational d → f transition from excited d state to ground state of Ce^{3+} ions (^{2}F$_{5/2}$, ^{2}F$_{7/2}$) split by the spin-orbit

coupling [35]. Under excitation with 230 nm, and 243 nm respectively (figure 6.19.d) the emission spectra reveals the all known Tb^{3+} lines situated in blue, green and red spectral domain specific for $^5D_4$ - ^7F_j (j= 6, 5, 4) transitions [35]. The chromatic map is presented in figure 6.20.a along with photos of samples under UV lamp [32]. When the phosphor is excited with 365 nm, UV radiation is absorbed and then transfered from $5d$ excited state of Ce^{3+} ions to $^5D_3$ excited state of Tb^{3+} ions. Low intensity emissions may occur in Tb^{3+} due to electronic transitions from $^5D_3$ to ^7F_J $_{(J = 6, 5, 4)}$ levels but being covered by the Ce^{3+} emission in the range 400÷450 nm. Some of the energy is transferred non-radiativelly between the $^5D_3$ and $^5D_4$ levels of Tb^{3+}. The electronic transitions betwin $^5D_4 \rightarrow {}^7F_{4, 5, 6}$ generate the well-known Tb^{3+} emissions, located in the spectral domains as follows: blue (487 nm, 498 nm), green (545 nm) and red (585 nm).

The chromatic map is presented in Figure 6.20.b, allong with photos of samples under UV light [32].
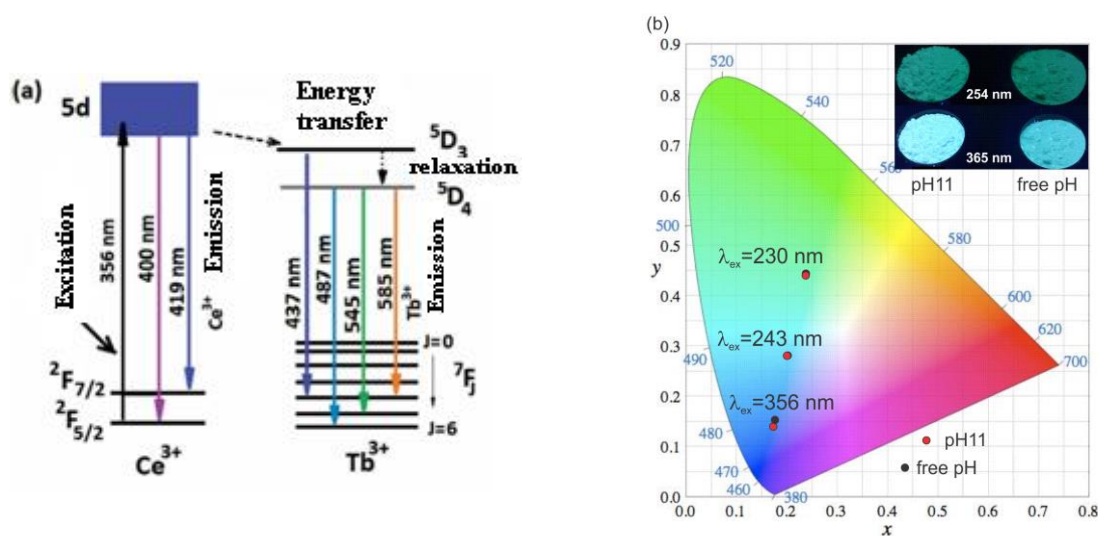
Figure 6.20. Schematic energy level diagram showing energy transfer between Ce^{3+} and Tb^{3+} in apatite lattice (a), Chromatic mapp and the eye perception of color under UV lamp of pH 11 and free pH samples (b)

The chromatic coordinates are placing the apatite samples in blue region (x= 0,175, y=0,141 for pH11 and x = 0,178, y = 0,155 for free pH) if excitation takes place with 356 nm; in the white- turquoise region (x= ,239 y= 0,449 for pH11 and x= 0,243, y= 0,453 for free pH) under excitation with 243 nm and in greenish region (x= 0,239 y= 0,449 for pH11 and x= 0,243, y= 0,453 for free pH) under excitation with 230 nm. For the same excitation radiation,

there is no significant difference between pH11 and free pH other than the intensity of the colour. Emission intensity of sample pH 11 is about three times higher than that of free pH. On the other hand, significant shift from blue to greenish is observed by changing the wavelength of excitation radiation.

7. ELECTRICAL PROPERTIES OF SILICATES WITH APATITE STRUCTURE

7.1 The effect of Bi^{3+} on the ionic conductivity of $La_{10}Si_6O_{27}$

This study shows the effect of Bi^{3+} and sintering temperature on the composition, structure and ionic conductivity of the apatites described by the formula: $La_{10-x}Bi_{x(}SiO_4)_6O_3$ (x = 0; 0,1; 0,15; 0,2; 0,3). Apatite powders were obtained at 1200^oC, 4h, and the ceramic pellets were uniaxial pressed (124 MPa) and sintering at 1400^oC, 6h. The sample doped with 1,5% Bi (x = 0,15) was also sintered at 1500^oC. The experimental amount of Bi, incorporated in the apatite lattice, was determined by ICP-OES measurements, an aspect that has not been discussed in the literature until now. The choice of the dopant ion was made taking into account the fact that Bi^{3+}, due to the electronic structure, can cause a high polarizability in the oxide lattice that can improve the mobility of O^{2-} ions, contributing to the increase of electrical conductivity [1]. Moreover, Bi^{3+} is used as a dopant in various oxidic systems to improve ionic conductivity and material sinterability [2,3]. In the literature are presented different types of apatite doped with Bi^{3+} that have conductivities in the range of $3,1 \cdot 10^{-6} \div 2,4 \cdot 10^{-5}$ $S \cdot cm^{-1}$, measured at 700^oC [4,5]. Through RSS, were obtained $La_{10-x}Bi_x(SiO_4)_6O_3$ apatite type (x = 0,5 $\div$ 2) with superior conductivities of $2,4 \cdot 10^{-4}$ $S \cdot cm^{-1}$ measured at 700^oC [6].

7.1.1 Structural characterization

XRD diffraction pattern presented in Figure 7.1, shows that all powders prepared contain pure apatite phase crystalized in hexagonal sistem [7]. The main diffraction line of the apatite structure descibed by the formula $La_{10}(SiO_4)_6O_3$, coresponding to PDF 530291, is centred at diffraction angle of $2\theta = 30,7^o$ and corespond to crystalline plane with Miller index [211].
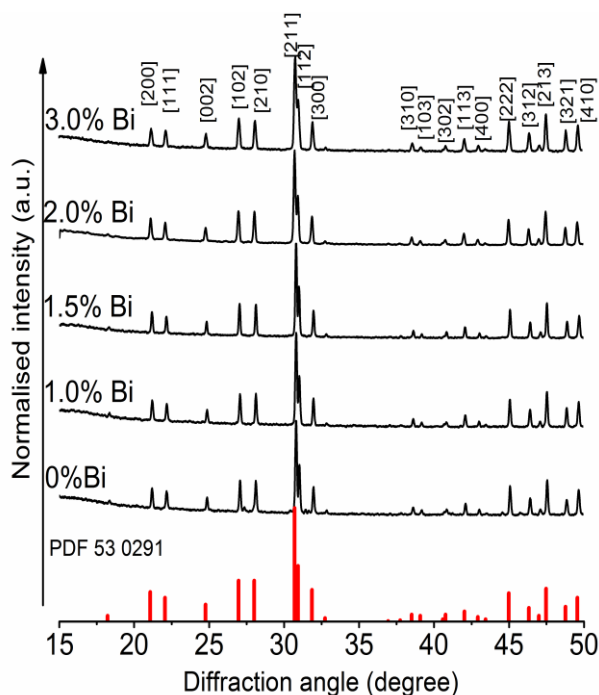
Figure 7.1. XRD difraction patterns of ceramics with apatite structure

To find out which of the hexagonal crystallographic systems fits best with the experimental powder diffraction patterns, several space groups have been tested: P63/m (176), P63 (173) and P-3 (147). Among them, the best fit was obtained for P-3 (147) according to ICSD 1526451 (a= b = 9,7248Å , c= 7,1895 Å, V= 588,831 Å^3) [8]. In order to provide crystallographic information about the lattice parameters, atomic positions and occupation factors the Rietveld refinement was performed using Reflex software from BIOVIA Materials Studio [9]. The structural refinement of apatite samples has been carried out using the Rietveld method, in order to find which positions of the La are occupied by Bi atoms. It was found that the best fit of the experimental powder diffraction patterns was obtained for the Bi atoms in the La3 position. In apatite with P-3(147) space group, La^{3+} ions can occupy different crystallographic sites: 9-coordinated La1/La2 (Wyckoff *2d*) and 7-coordinated La3 (Wyckoff *6g*) [8]. The ionic radius of La^{3+} in La1 and La2 is 1,216 Å and in La3 is 1,1 Å respectively [10]. The fitting of the XRD patterns for the 1,5 % Bi sample sintered at 1400°C is shown in Figure 7.2.a, along with atoms arrangements in the vicinity of O5-O6 channel (Figura 7.2.b) and   coordination environment of La1, La2 and La3 sites (Figura 7.2.c) [7]. It can been seen that La1 in *2d* site is surrounded by three O1, three O2, three O3; La2 in *2d* sites is surrounded by four O1, three O2 , two O4 while La3 in 6g site is surrounded by one O1, one O2 , two O3, one O4 and free-oxygens O5, O6.

The refined structural parameters are summarized in Table 7.1 [7]. The lattice parameters do not significantly change with Bi doping level because the ionic radii of La^{3+} and Bi^{3+} are practically equal (1.03 Å for CN= 6) [10].
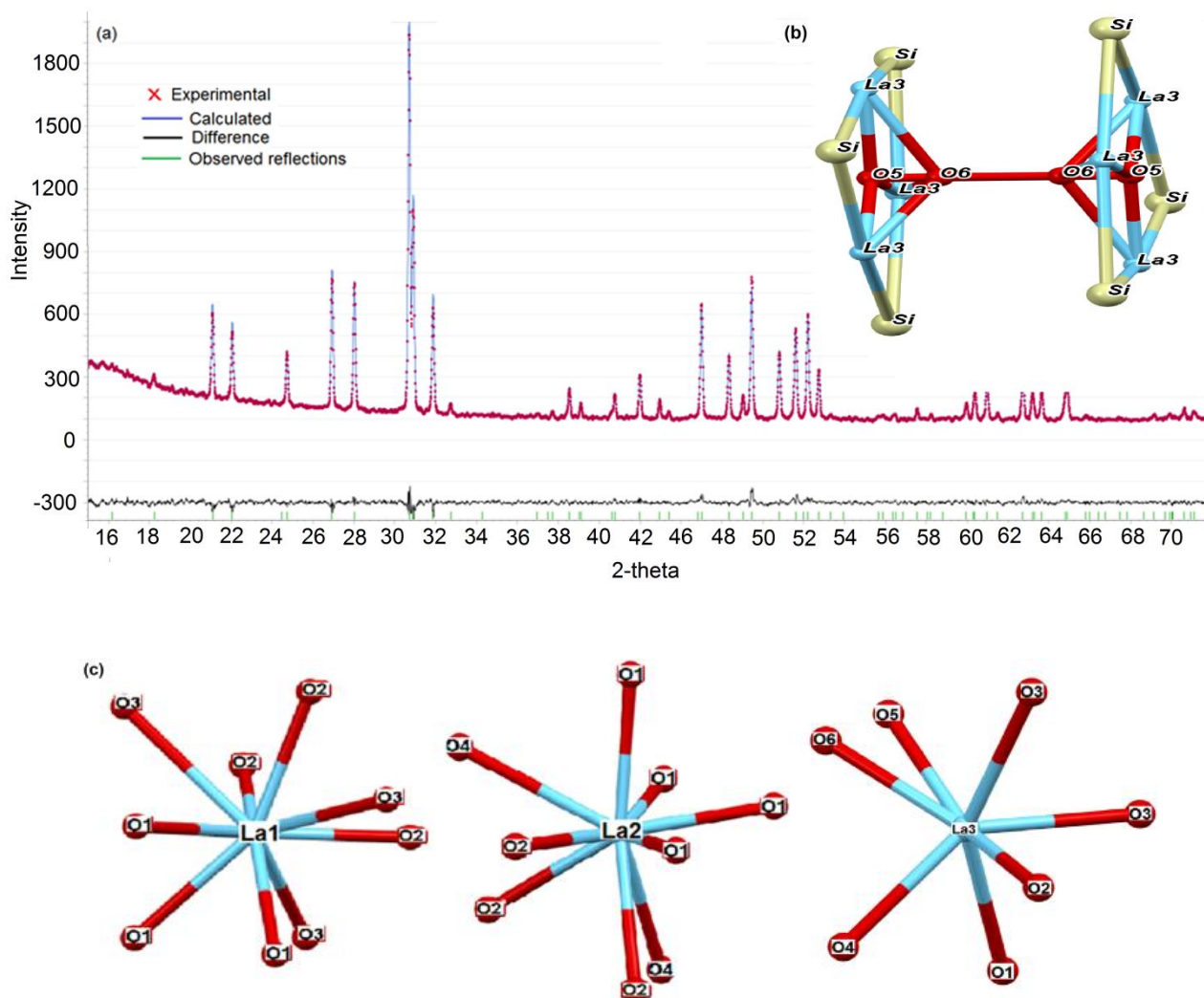
Figure 7.2 Experimental (crosses) and calculated (blue solid line) powder XRD pattern of 1,5 % Bi^{3+} apatite - sintered at $1400^{o}C$ (a); arrangements of atoms in vicinity of oxigen chanel (inset b). The coordination environment of La^{3+} sites (c)

The effective crystallite mean size (D_{eff}) and the root mean square of the microstrains (ε) were also calculated on the basis of XRD diffractograms. The crystallite sizes and microstrains were evaluated using Williams-Hall plot [11] and are listed in Table 7.1, along with theoretical densities obtained from the lattice parameters (D_t), the measured densities (D_m) and the relative densities (D_r). The thermal treatment of samples done at $1400^{o}C$, 6h

leads to densities between 79,41 % and 87,09 %. However, the density was increased up to 91.63 % when sample doped with 1.5% Bi is sintered at $1500^{o}C$, 6h. Samples doped with 1.5% Bi presents the largest crystallite size (95,2 nm at $1400^{o}C$ / 118 nm at $1500^{o}C$) and the lowest values of micro strains (4,04 at $1400^{o}C$ /3,30 at $1500^{o}C$) depending on the sintering temperature.

Table 7.1. Refined structural parameters and densities of apatite pellets

Lattice parameters	Bismuth theoretical doping level (%) [1]					
	0,0	1,0	1,5	1,5 *	2,0	3,0
a = b (Å)	9,723	9,724	9,721	9,725	9,725	9,721
c (Å)	7,187	7,190	7,195	7,189	7,190	7,192
V ($Å^3$)	588,497	588,820	588,813	588,822	588,831	588,604
R_p (%)	4,45	3,72	3,29	3,79	2,63	3,38
R_{wp} (%)	6,07	4,84	4,21	5,45	3,35	4,35
F_{occ} O5	1,000	0,988	0,905	0,828	0,998	1,000
F_{occ} O6	0,239	0,293	0,197	0,128	0,078	0,432
D_{eff} (nm)	86	83	95	118	74	58
$\varepsilon \cdot 10^{-4}$ (%)	5,520	5,170	4,070	3,300	5,300	7,200
D_m (g/cm^3)	4,889	4,530	4,581	5,155	4,428	4,490
D_t (g/cm^3)	5,614	5,622	5,327	5,626	5,630	5,654
D_r (%)	87,09	80,58	81,41	91,63	78,65	79,41

Sample sintered at $1500^{o}C$; [1] reported at 10 moles La

7.1.2 Morphology and chemical composition by SEM, ICP-OES and XPS

The morphologies of apatite pellets were studied using the scanning electron microscopy and illustrated in Figure 7.3 [7]. It can be observed that the homogeneity and compactness of the ceramics depends on the Bi doping level. Un-doped apatite is presented as a well densified mass of homogeneous rounded grains but with undefined surface as if presenting very fine ribs. The grain size varies between 1.0 μm to 2.5 μm. Doping of apatite with 1.5% Bi leads to a quite dense material with low porosity consisting of well formed slightly elongated grains with clean and compact grain boundaries. The main feature of 3% Bi doped apatite is the presence of increased porosity and a rough surface, mainly from lack of well-defined grains, most probably due to a higher Bi_2O_3 volatilization. This feature is confirmed by the lower density of the sample (4,49 g/cm^3) in comparison with samples 0% Bi (4,889 g/cm^3) and 1,5% Bi (4,58 g/cm^3), sintered at $1400^{0}C$.
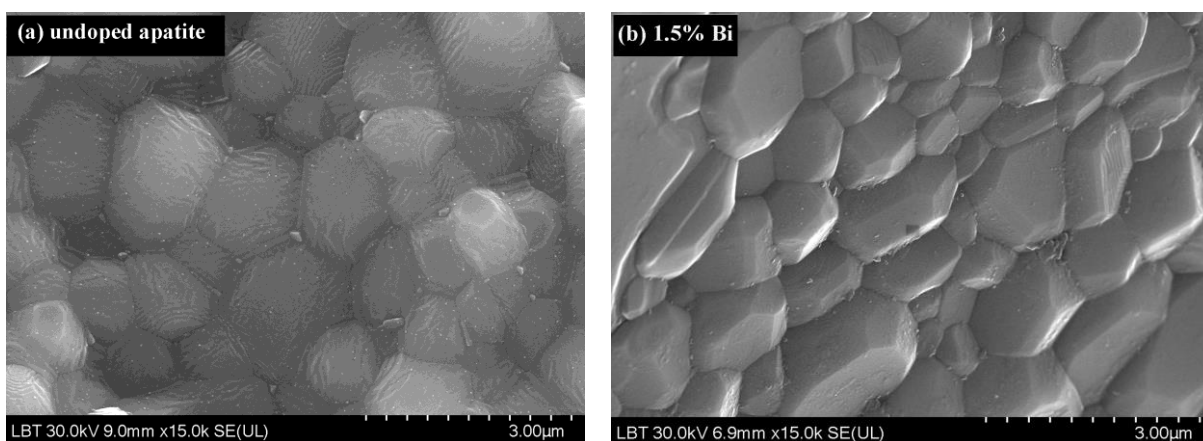
Figure 7.3. SEM pictures of apatite type ceramicics, un-doped (a) and Bi doped (b), sintered at 1400°C

The Bi content was determined (experimental by ICP-OES) and is approximately twice lower than the theoretical value, which is most likely due to volatilization during heat treatments [12]. Formation of these volatile compounds, contribute to an advanced, uniform dispersion of the Bi in the host lattice. Theoretical and experimental ICP results along with apatite formulas are systematized in Table 7.2 [7].

Table 7.2. Theoretical and experimental composition of apatites
based on experimental La-Bi values

Sample code	Theoretical data			ICP-OES experimental data			
	Apatite formula	La_{theor} (mg	Bi_{theor} (mg)	La_{exp} (mg)[•]	Bi_{exp} (mg)[•]	Apatite formula	Bi (mole)
0,0 % Bi	$La_{10}(SiO_4)_6O_3$	34,92	0,00	35,09	0,00	$La_{10,04}(SiO_4)_6O_{3,06}$	0,00
1,0 % Bi	$La_{9,9}Bi_{0,1}(SiO_4)_6O_3$	34,44	0,52	34,10	0,29	$La_{9,80}Bi_{0,06}(SiO_4)_6O_{2,79}$	0,06
1,5 % Bi	$La_{9,85}Bi_{0,15}(SiO_4)_6O_3$	34,20	0,78	34,56	0,41	$La_{9,95}Bi_{0,08}(SiO_4)_6O_{3,04}$	0,08
2,0 % Bi	$La_{9,8}Bi_{0,2}(SiO_4)_6O_3$	33,97	1,04	35,31	0,53	$La_{10,18}Bi_{0,10}(SiO_4)_6O_{3,42}$	0,10
3,0 % Bi	$La_{9,7}Bi_{0,3}(SiO_4)_6O_3$	33,51	1,56	33,99	1,08	$La_{9,84}Bi_{0,21}(SiO_4)_6O_{3,07}$	0,21

[•] *coresponding to 0,05 g sample*

It is observed that the sample doped with 1,5% Bi has the composition closest to the theoretical formula.

XPS analysis was performed to determine the chemical states of each element in the 1,5% Bi apatite sample. The data were analyzed by using Casa XPS software. Core-levels of La 3*d*, Bi 4*f* and Si 2*s* were recorded and their quantification is shown in Figure 7.4 [7].
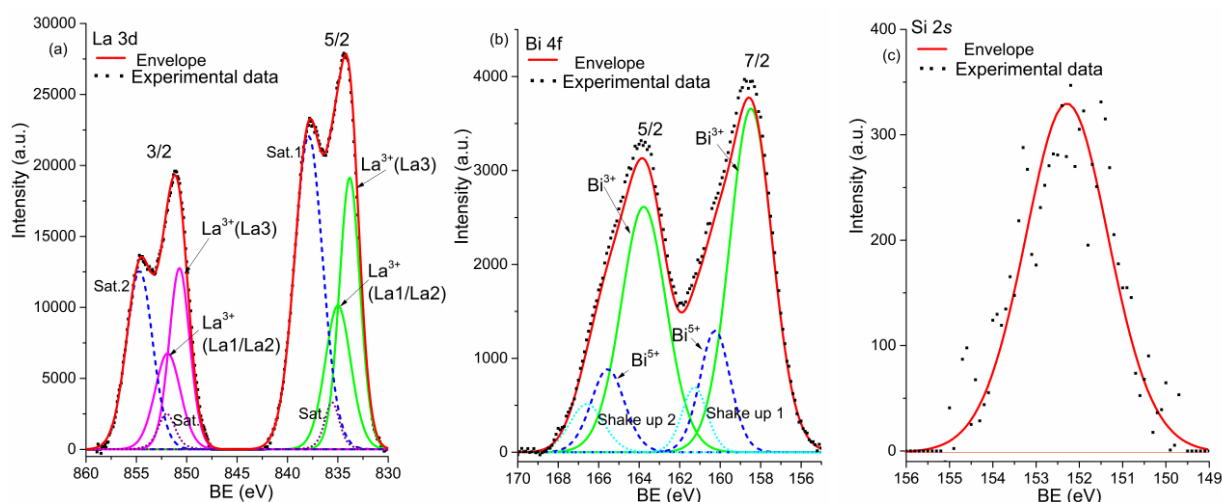
Figure 7.4. The XPS spectra of La 3d (a) , Bi 4f (b) and Si2s (c) core-level for the 1,5 % Bi apatite sintered at 1500°C and the corresponding deconvolutions and fitted curves

A linear background was extracted for La 3*d* lines while a Shirley type one was considered in case of Bi 4*f* and Si 2*s* core-level spectra. In the specific case of lanthanum 3*d* the experimental data were fitted by using two parent lines positioned at 837,7eV; 834,3eV and 854,5 eV; 851,1 eV for each component of the 5/2, 3/2 doublet respectively.   They correspond to the two inequivalent positions of La inside the apatite unit cell. Additionally two shake-up satellite line were considered for each doublet component. They represent envelopes which accounts for the usual multiplet splitting of the La 3*d* core-level line.

Regarding the Bi 4*f* also two inequivalent positions of was found at binding energies of 158,6 eV and 163,8eV for 7/2 and 5/2 spin-orbit doublet components respectively. They are associated to Bi^{3+} and Bi^{5+} states accordingly. Also two shake-up satellite features, corresponding to photoelectrons energy loss associated to the excitation of an additional electron from the valence band into the conduction band, are also seen in the spectrum. Since the Si 2*p* core-level spectrum, usually used in XPS analyses, is overlapped by the La 4*d* spectrum, we focused on recording the Si 2*s* core level. The spectrum is shown in Fig. 2c and, as expected, is positioned at a binding energy of 15,3 eV.

7.1.3 Electrical conductivity

To perform ionic conductivity measurements, apatite powders were pressed at 127 MPa and then sintered in air in order to obtain ceramic pellets. On both surfaces of the ceramic pellets was applied a conductive Ag paste, with the role of electrode and fixed by treatment at 400°C, 1h. The conductivities of the apatite pellets were analyzed by EIS

technique and measured in the temperature range of 300÷600°C, with an increment of 50°C, in air. The impedance measurements highlight the bulk, grain boundary and electrode processes by exhibiting corresponding RC circuits in complex plane representations [13]. Figure 7.5 shows the typical impedance Nyquist spectra of apatite samples sintered at 1400°C, measured at 500°C, using Nyquist plots.
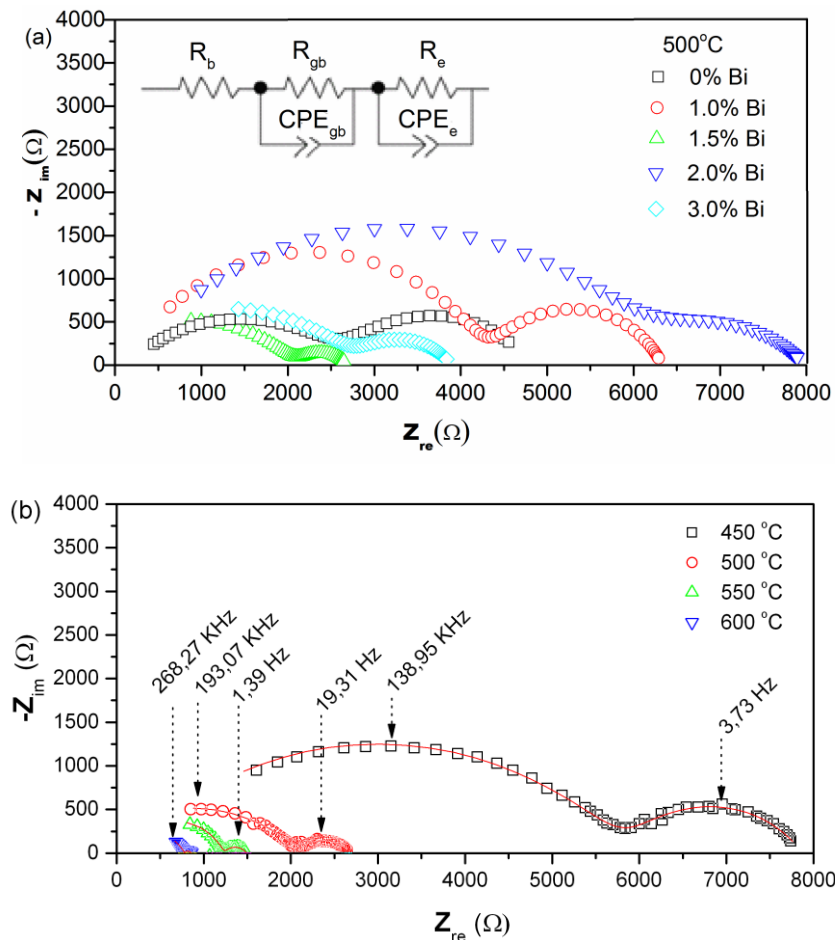
Figure 7.5. Nyquist plots of impedance for apatites pellets sintered at 1400°C, measured at 500°C, inset - equivalent electrical circuit(a); influence of temperatures on impedance of 1,5% Bi doped sample sintered at 1400°C (b)

It can be seen that the sample doped with 1,5% Bi exhibits the lowest resistances of elementary processes, an indication of improved conductivity [7]. The impedance spectra consist in two distorted semicircles. The high frequency semicircle with capacitance value of $C_{gb}=1,97 \cdot 10^{-10}$ F (for 1,5% Bi sintered at 1400°C) is associated with grain boundary response which is in concordance with reported studies [14]. Similarly, in the case of low frequency semicircle the capacitance value $C_e=1,11 \cdot 10^{-5}$ F (for 1,5% Bi sample) can be identified as the

contribution of electrochemical processes taking place at metal surface. Because the reported capacitance of bulk phase is in 10^{-12} F range, the contribution of bulk phase conductivity is included in the series resistor R_b of the electrical equivalent circuit, together with the much smaller contribution of electrical wires and contacts [14]. The electrical equivalent circuit, Figure 7.5.a, contains along with bulk, grain boundary and electrode resistances (R_b, R_{gb}, R_e) two constant phase elements (CPE_{gb}, CPE_e) in order to allow the fitting of imperfect RC circuits. The results of fitting procedure for 1,5% Bi sample are presented in Table 7.3 [7]. The influence of temperature on impedance for 1,5% Bi sample sintered at 1400°C is presented in Figure 7.5.b. One can see that the impedance decreases with temperature.

Tabel 7.3. Fitting parameters at different tempreatures for $La_{9,85}Bi_{0,15}Si_6O_{27}$
apatite pellets sintered at 1400°C

Temperature (°C)	R_b (Ω)	R_{gb} (Ω)	R_e (Ω)	CPE_{gb} (F)	CPE_e (F)
350	$1,08 \cdot 10^3$	$4,41 \cdot 10^4$	$1,88 \cdot 10^4$	$1,04 \cdot 10^{-10}$	$6,45 \cdot 10^{-7}$
400	$7,32 \cdot 10^2$	$1,87 \cdot 10^4$	$5,35 \cdot 10^3$	$1,27 \cdot 10^{-10}$	$1,16 \cdot 10^{-5}$
450	$4,21 \cdot 10^2$	$5,73 \cdot 10^3$	$2,01 \cdot 10^3$	$1,74 \cdot 10^{-10}$	$7,33 \cdot 10^{-6}$
500	$3,18 \cdot 10^2$	$2,51 \cdot 10^3$	$6,82 \cdot 10^2$	$1,97 \cdot 10^{-10}$	$1,11 \cdot 10^{-5}$
550	$2,82 \cdot 10^2$	$1,12 \cdot 10^3$	$2,61 \cdot 10^2$	$2,17 \cdot 10^{-10}$	$1,10 \cdot 10^{-5}$
600	$1,03 \cdot 10^2$	$6,78 \cdot 10^2$	$7,86 \cdot 10^1$	$1,81 \cdot 10^{-10}$	$2,23 \cdot 10^{-5}$

The total conductivity is calculated using the thickness to area ratio (L/S) of each sample, according to equation 7.1 [15].

$$\sigma_{Tot} = \frac{L}{(Rb + Rgb) \times S} \qquad 7.1$$

The values of conductivities are presented in Table 7.4 along with pre-exponential factor and activation energy in apatite lattice [7]. Ionic conductivity is influenced by the mobility of O^{2-} ions, which in turn depends on the structural disorder in the apatite lattice [16]. In this case, the conductivity of sintered apatites at 1400°C increase from $6,46 \cdot 10^{-5}$ S·cm^{-1} (0,0% Bi) to $9,22 \cdot 10^{-5}$ S·cm^{-1} (1,5% Bi) then decreasses at $5,08 \cdot 10^{-5}$ S·cm^{-1} (3,0% Bi). The variation in the ionic conductivity of apatites can be attributed to lattice defects, which can affect the migration of interstitial O^{2-} ions depending on the Bi doping level.

Table 7.4. Conductivities at 500^oC, pre-exponential factors and activation energies
of ionic conductivity for Bi doped apatites

Sample code	Apatite Bismuth content (mole)		L/S (cm^{-1})	$\sigma_{500}{}^o{}_C$ ($S{\cdot}cm^{-1}$)	σ_o ($S{\cdot}K{\cdot}cm^{-1}$)	E_a (eV)
	Theoretic	Experimental [1]				
0,0% Bi	0,00	0,00	0,195	$6,46{\cdot}10^{-5}$	$3,15{\cdot}10^4$	0,89
1,0% Bi	0,10	0,06	0,202	$3,89{\cdot}10^{-5}$	$1,44{\cdot}10^4$	0,86
1,5% Bi	0,15	0,08	0,260	$9,22{\cdot}10^{-5}$	$2,16{\cdot}10^4$	0,84
1,5% Bi*	0,15	0,08	0,445	$1,02{\cdot}10^{-3}$	$4,20{\cdot}10^4$	0,77
2,0% Bi	0,20	0,10	0,217	$3,33{\cdot}10^{-5}$	$1,11{\cdot}10^4$	0,87
3,0% Bi	0,30	0,21	0,197	$5,08{\cdot}10^{-5}$	$1,76{\cdot}10^4$	0,88

L- pellet thick; S- electrode area; sample sintered at 1500^oC; [1] from ICP*

The Bi concentration does not influence significantly the conductivity of samples sintered at 1400^oC since the values are situated in a narrow range ($3,89{\cdot}10^{-5}$ Scm^{-1} and $9,22$ ${\cdot}10^{-5}$ Scm^{-1}). Sintering temperature has a much stronger influence on conductivity since sintering the 1,5% Bi apatite pellet at 1500^oC leads to a significant increase of the relative density from 81,41% to 91,63% and improve the conductivity from $9,22{\cdot}10^{-5}$ Scm^{-1} to $1,02$ ${\cdot}10^{-3}$ Scm^{-1} (at 500^0C). We found that, our conductivity value is higher than that reported in literature ($1,46{\cdot}10^{-4}$ Scm^{-1} at 650^oC) [5]. According to Rietveld refinement samples with the highest conductivities (1,5% Bi and 1.5% Bi*) present the lowest occupation factors for O5 and O6, suggesting the presence of oxygen vacancies (Table 7.1). On the other hand, the ICP measurements indicate a slightly higher oxygen excess probably randomly distributed in apatite lattice; oxygen which could not be identified by XRD since does not occupy fixed positions. It is possible that Bi^{5+} identified in 1,5% Bi sample sintered at 1500^oC (fig 5b) generates cationic excess and induce some interstitial oxygen around La3 position which may be involved in conduction. Certain contribution to conduction may be given by the micro-structural parameters (D_{eff} and ε) since both 1,5% Bi samples present the largest crystallite size and the lowest values of micro strains (Tabel 7.1). Above mentioned facts may explain the higher conductivity of samples 1,5% Bi sintered at 1400^oC and 1500^oC respectively. The temperature dependence of conductivity was analyzed using the Arrhenius equation 7.2 [15]:

$$\sigma{\cdot}T = \sigma_o \exp\left(-\frac{Ea}{kB*T}\right) \qquad 7.2$$

where: σ - conductivity, σ_o - pre-exponential factor related to concentration of mobile O^{2-} ion, E_a - activation energy for conduction, k_B - Boltzmann constant and T - absolute temperature.

The Arrhenius plots for each composition together with the fitting lines are presented in Figure 7.6 [7].
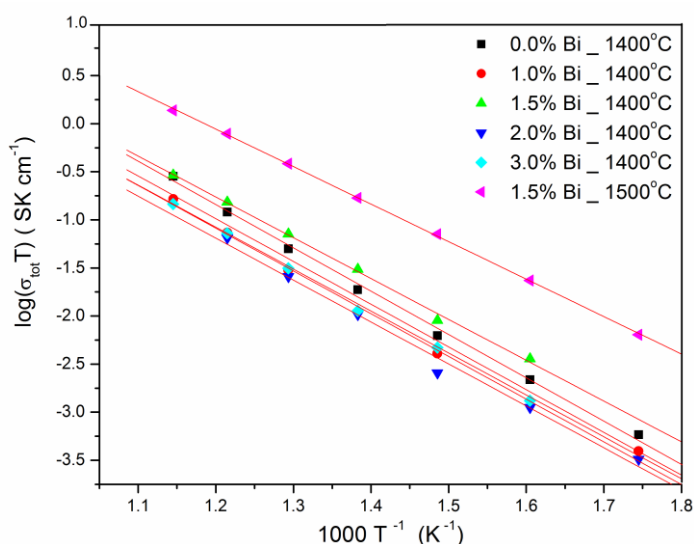
Figure 7.6. Arrhenius plots of total conductivity for Bi doped apatite ceramics

The influence of temperature on the conductivity indicates that the migration of oxide ions is thermally activated and depends upon the apatites composition. The activation energy values obtained in this study are close to the values reported in literature [5,16].

GENERAL CONCLUSIONS

In this thesis, **73 apatite samples** were prepared by different synthesis methods and doped with different cations (rare earth, transitional and post-transitional) which give improved special properties, compared to other similar materials presented in the literature. The luminescent and electrical properties of apatites are influenced by the synthesis methods same as the preparative conditions. The evidence of all samples is summarized in Annex 4.

Apatites with luminescent properties (62 samples) were obtained by: Solid state reaction, Precipitation, Combustion and Sol-Gel methods.

* Pure apatite phase was obtained by the Solid state reaction either by slow calcination at 1200°C, 240' or by rapid calcination at 1400°C, 30'. A pronounced increase of

crystallite size was observed with the calcination temperature, from 74 nm (1000oC) to 217 nm ($1400^{o}C$) and a less significant one, from 137 nm (30') to 152 nm (480'), with duration of calcination. The photoluminescent (FL) and cathodoluminescent (CL) emissions of the samples, in the green spectral range, have the maximum located at 544 nm, attributed to the electronic transitions $^{5}D_{4} \rightarrow ^{7}F_{5}$ in Tb^{3+} ions. Both emissions show an increase in intensity up to $1200^{o}C$, followed by a decrease between $1200 \div 1400^{o}C$. The highest intensities of FL and CL were obtained by calcination of the precursor at $1200^{o}C$, 30', due to additional radiative processes, which ocurs in secondary $Y_{2}O_{3}$ phase, found in apatite lattice. Various precipitating agents were tested in order to obtain apatite through mW-assisted precipitation, namely: oxalic acid, citric acid, ureea, ammonia, sodium hydroxide, sodium carbonate. Among them, only sodium hydroxide led to apatite phase. The stoichiometric ratio between the reactants (NO^{3-}: TEOS = 1: 0,6) is not optimal to obtain the pure apatite phase. In the samples, $Y_{2}SiO_{5}$ and $Y_{2}O_{3}$ were identified as secondary phases.

* The precipitation degree is considerably influenced by the pH, due to the variety of cations involved (Ca^{2+}, Y^{3+}, Ce^{3+}, Tb^{3+}), which have different precipitation rates and solubility products. The precipitation degree of calcium (46,5%) increase with the increase of pH from 7 to 11. Yttrium precipitates almost completely, regardless of the reaction medium. Therefore the composition of the precursors is affected leading to variable compositions and cristalinity degree. The main component in precursors is yttrium hydroxy nitrate, with a degree of crystallinity of 36% at pH 7. Yttrium carbonate phase occurs with increasing of pH to 11 and with decrease of crystallinity to 6% . The precursors lose their porosity and become completely crystalline by heat treatment. Under stoichiometric conditions the phosphors contain 98% $Y_{2}O_{3}$ (pH 7) and a mixture of 27% $Y_{2}O_{3}$ and 73% $Y_{2}SiO_{5}$ (pH 9), respectively. At pH 11 and free pH, the major component is the apatite phase, and $Y_{2}O_{3}$ appears as traces.

* Excess of TEOS: 50% in microwave-assisted synthesis and 40% in simple precipitation, contributes to the removal of the secondary phase of $Y_{2}O_{3}$. Samples prepared with 25%, 35%, 45% TEOS excess leads to $Y_{2}O_{3}$ and $Y_{2}SiO_{5}$ secondary phases. The pure apatite phases are obtained only at pH 11 and free pH, with a molar excess of 40% TEOS. The luminescence of apatites is indirectly affected by the pH during precipitation, through structural changes. Samples with impure structure (pH 7, pH 9), have a low excitability and a low emission intensity. Precipitation at pH 11 with 40% TEOS excess leads to a silicate with a pure apatite structure, with an emission intensity 3,6 times higher than that of apatite

obtained at free pH and 18 and 46 times higher than of samples prepared at pH 9 and pH 7. The chromatic coordinates of apatites obtained at pH 11 and free pH vary from blue (λex = 356 nm), to turquoise (λem = 243 nm) and green (λex = 230 nm) depending on the excitation wavelength.

　　　* The morphology and structural purity of the apatite powders obtained by mW-assisted precipitation is influenced by the nature of the host lattice. Precipitation in the Ca-La system leads to the formation of powders with pure apatite structure starting with the temperature of $1100^{o}C$, while precipitation in the Ca-Y system provides apatites impurified with Y_2O_3 and Y_2SiO_5 even at high temperatures ($1400^{o}C$). A composition close to the theoretical one was obtained in the case of CYSO apatites, with slightly higher Y values than the theoretical ones, explained by the presence of Y_2O_3 as secondary phase. In the Ca-La system, the Ca content is half of the theoretical one, indicating a change in the stoichiometry of the final reaction product as a result of the redissolution of $Ca(OH)_2$. The increase of the calcination temperature from $800^{o}C$ to $1400^{o}C$, directly influences: ▸the degree of Tb^{3+} incorporation, which increases between 0,101-0,122 moles in CYSO, respectively between 0,108-0,115 moles in CLSO; ▸micro-strains in the crystal lattice, which decrease significantly from $15,44 \cdot 10^{-4}$ to $3,68 \cdot 10^{-4}$ (CYSO) and from $14,09 \cdot 10^{-4}$ to $4,24 \cdot 10^{-4}$ (CLSO); ▸powder porosity, which decreases from 0,336 cm^3 /g to 0,003 cm^3 /g (CYSO), respectively from 0,063 cm^3 /g to 0,020 cm^3 /g (CLSO); ▸ crystallites sizes, which increase from 26,1-103,2 nm (CYSO) and 60,8-105,0 nm (CLSO). The excitation spectra of the samples shows the formation of a single Tb^{3+} emission center (235 nm) in La phosphors and multiple emission centers in Y-based phosphors, (235 nm, 246nm, 276 nm, 303 nm) due to the partial incorporation of Tb^{3+} ions in the Y_2O_3 lattice, formed as a secondary phase. The degree of Tb^{3+} incorporation in CYSO is higher than in CLSO, which explains the lower luminescence of CLSO. The chromatic coordinates of the phosphors are in the green (CYSO) and turquoise (CLSO) range.

　　　* The host lattice has a major influence on phase purity in the case of apatites obtained by *Combustion*. The La apatite sample is slightly contaminated with traces of La_2SiO_5, while the Y lattice has a high secondary phases content of Y_2O_3, Y_2SiO_5 and $Y_2Si_2O_7$.

　　　* Substitution of alkali metal cations (Ca^{2+}, Mg^{2+}) into the Y host lattice leads to the formation of pure apatite phases. The photoluminescent excitation spectra of YAp: Bi and LaAp: Bi have the same intensity at ~ 304 nm, unlike MgYAp: Bi which has a 2 times higher

intensity. Excitation maxima from 226 nm and 304 nm are assigned to transitions $^1S_0 \rightarrow {}^3P_1$ in Bi^{3+} (II) and Bi^{3+} (I) ions, respectively. Accomodation of Mg into the YAp lattice creates a new position for the incorporation of Bi^{3+} ions and causes a contraction of the lattice, due to the lower ionic radii of Mg^{2+} compared to Y^{3+}. Lattice distortion generates an excitation band at 372 nm (potential applicative in LEDs area). The ratio of the emission bands at 420 nm and 465 nm remains unchanged for Y-based apatites, demonstrating the preference of Bi^{3+} ions to incorporate in position I in the lattice. The maximum emission of LaAp shifts to 442 nm, as a result of structural changes given by La^{3+} ions whose ionic radii are larger than those of Y^{3+}. The emission intensity also increases to 465 nm, changing the ratio between the two bands.

* The emission color of apatites can be modulated by the activator ions. Doping with Ce^{3+} leads to a blue luminescence (λem = 406 nm, λem = 469 nm), due to the electronic transitions $5d \rightarrow {}^2F_j$ /2; j = 5,7. Doping with Tb^{3+} generates a green luminescence (λem = 544 nm), due to the predominance of $^5D_4 \rightarrow {}^7F_5$ transitions. Eu^{3+} ions generate $^5D_0 \rightarrow {}^7F_j$ transitions, located in the red spectral range (λem = 615 nm), and Bi^{3+} in the blue range (λem = 442 nm, λem = 465 nm), as a result of $^1S_0 \rightarrow {}^3P_1$ electrons transitions.

* Concentration of the activator ion influences the emission intensity of apatites. Doping with Ce^{3+} generates maximum values of emission intensity at 1,5% Ce^{3+} (λex = 321 nm) and 6,0% Ce^{3+} (λex = 362 nm). Bi^{3+} doping produces a maximum emission intensity at 1,5% Bi^{3+} (λex = 301 nm).

* The phase of pure hexagonal apatite is formed only by using Combustion and Sol-Gel method. The correlations between the compositions and the luminescent behavior of the samples obtained by the 4 methods reveal two interesting features: (1) the appearance of a new excitation band at 360 nm, only in the samples obtained by *Precipitation*, associated with the incorporation of Ce^{3+} in the secondary Y_2SiO_5 monoclinic phase; (2) displacement of the Ce^{3+} band from 406 nm in the pure sample (Combustion) to 400 nm in the impure apatite sample (Stoichiometric precipitation). 50% TEOS excess in *Precipitation*, leads to the transformation of the Y_2O_3 phase into monoclinic yttrium silicate, increasing the Ce^{3+} emission which becomes 8 times higher than in the case of *Stoichiometric Precipitation* and 3 times higher than in *Combustion*. The emission spectra are similar in shape, but different in intensity and consist of the contribution of both types of transitions: $5d \rightarrow 4f$ in Ce^{3+} and $^5D_4 \rightarrow {}^7F_J$ in Tb^{3+}. Apatites have a turquoise luminescent emission, which moves to the blue region when the excitation radiation decreases from 321 to 231 nm.

Apatites with electrical properties (11 samples) were obtain by *Combustion.*

■ Bi^{3+} doping of lanthanum silicate led to pure apatite structures, with a P6-3 type spatial group (147). The crystallite size varies between 57,9-118,0 nm, depending on the Bi^{3+} doping level and the sintering temperature. The incorporation of Bi^{3+} in the apatite lattice is ~ 2 times lower than the theoretical value, due to the volatilization of Bi_2O_3 during thermal processes. The presence of Bi^{5+} in the 1,5% Bi - 1500°C was also identified, which creates an excess of positive charge that can induce interstitial oxygen, helping in conduction. The level of Bi doping does not significantly influence the conductivity of the sintered samples at 1400°C, which varies between $3,89 \cdot 10^{-5}$ S·cm^{-1} and $9,22 \cdot 10^{-5}$ S·cm^{-1}. The sintering temperature greatly influences the relative density of the samples which increases from 81,41% (1,5% Bi-1400°C) to 91,63% (1,5% Bi-1500°C), contributing to the increase of conductivity from $9,22 \cdot 10^{-5}$ S·cm^{-1} at $1,02 \cdot 10^{-3}$ S·cm^{-1} (at 500°C).

■ By doping with Cr^{3+}, Fe^{3+}, Mn^{4+}, Mo^{6+}, W^{6+} at the Si^{4+} cation, apatite-type ceramics with a P6$_3$/m spatial group were obtained. FeAp and WAp samples contain a single crystalline phase of apatite, while MnAp, CrAp, MoAp samples contain a secondary phase of La_2SiO_5 as traces. Sintering at 1400°C leads to relative densities between 87,55% (Mn^{4+}) and 89,03% (Cr^{3+}). Differences between the ionic radii of the doping cations and Si^{4+} can cause distortions of the silicate network directly influencing the conductivity of apatites. Moreover, the incorporation of aliovalent cations at the Si^{4+} position leads to nonstoichiometric apatites with oxygen vacancies. The existence of a disordered crystalline environment and oxygen vacancies (Cr^{3+}, Fe^{3+}), improve ionic conductivity, the corresponding apatites recording the highest conductivities in the series ($\sigma_{550oC} = 6,326 \cdot 10^{-4}$ S·cm^{-1} for CrAp; $\sigma_{550oC} = 5,050 \cdot 10^{-4}$ S·cm^{-1} for FeAp; compared to $\sigma_{550oC} = 2,574 \cdot 10^{-4}$ S·cm^{-1} for WAp).

Bibliografie selectivă

Capitol 4:

[1] F. Deganello, A. K. Tyagi, Solution combustion synthesis, energy and environment: Best parameters for better materials, Progress in Crystal Growth and Characterization of Materials 64 (2018) 23-61

[2] Y. Zhang, G.C. Stangle, Preparation of fine multicomponent oxide ceramic powder by a combustion synthesis process, Journal of Materials Research and Technology 9 (1994) 1997-2004

Capitol 5:

[7] D. Kioupis, M. Argyridou, A. Gaki, G. Kakali, Wet chemical synthesis of $La_{9,83-x}Sr_xSi_6O_{26+\delta}$ ($0\leq x\leq0.50$) powders, characterization of intermediate and final products, Journal of Rare Earths 33 (2015) 320-326

[12] J. A. Aric, Infrared spectra of minerals and related inorganic materials, Butterworths, London, UK (2016)

[14] I. Perhaita, L. E. Muresan, D. T. Silipas, L. B. Tudoran, Comparative study on blue-turquoise silicate apatite phosphors prepared via different synthesis routes, Journal of Sol-Gel Science and Technology 89 (3) (2019) 807-819

[28] I. Perhaita, L. E. Muresan, L. Barbu Tudoran, D. T. Silipas, G. Borodi, Synthesis of silicate apatite phosphors with enhanced luminescence via optimized precipitation technique through pH control, Journal of Sol-Gel Science and Technology (2020) doi.org/10.1007/s10971-020-05400-1

[31] L. T. K. Giang, T. K. Anh, L. Marciniak, D. Hreniak, W. Strek, W. Lojkowski, L. Q. Preparation and characterization of Yttrium hydroxide and oxide doped with rare earth ions (Eu^{3+}, Tb^{3+}) nano one dimensional, Physics Procedia 76 (2015) 73-79

[44] T. Kharlamova, O. Vodyankina, A. Matveev, V.Stathopoulos, A. Ishchenko, D. Khabibulin, V. Sadykov, The structure and texture genesis of apatite-type lanthanum silicates during their synthesis by co-precipitation, Ceramics International 41 (2015) 13393-13408

[45] Shannon-Prewitt, Effective ionic radius navigation program

Capitol 6:

[26] I. Perhaita, L. E. Muresan, D. T. Silipas, L. Barbu Tudoran, Comparative study on blue-turquoise silicate apatite phosphors prepared via different synthesis routes, Journal of Sol-Gel Science and Technology (2019) doi.org/10.1007/s10971-018-4911-8

[32] I. Perhaita, L. E. Muresan, L. Barbu Tudoran, D. T. Silipas, G. Borodi, Synthesis of silicate apatite phosphors with enhanced luminescence via optimized precipitation technique through pH control, Journal of Sol-Gel Science and Technology, doi.org/10.1007/s10971-020-05400-1

[34] R. Yu, H. Li, H. Ma, C. Wang, H. Wang, A new blue-emitting phosphor of Ce^{3+} activated fluorosilicate apatite $Ba_2Y_3[SiO_4]_3F$, Journal of American Ceramic Society 97 (2014) 1151-1156.

[35] G. Blasse, B. C. Grabmaier, Luminescent Materials, Springer-Verlag (1994)

[36] V. Singh, N. Singh, M.S. Pathak, P.K. Singh, V. Natarajan, Tb^{3+} doped $Ca_2La_8(SiO_4)_6O_2$ oxyapatite phosphors, Optik, 171 (2018) 356-362

Capitol 7:

[4] M. Abbassi, R. Ternane, I. Sobrados, A. Madani, M. Trabelsi-Ayadi, J. Sanz, Synthesis, characterization and oxide conduction in Ba doped apatite-type silicates $Ca_2La_6Bi_2(SiO_4)_6O_2$, Materials Chemistry and Physics 147 (2014) 285-292

[7] I. Perhaita, L.E. Muresan, A. Nicoara, L. Barbu Tudoran, G.Borodi, L. M. Muresan, Morpho-structural and electrical characterization of Bi doped apatite type lanthanum silicates prepared by gel-combustion, Applied Physics (2020)

[12] D. Xu, X. Cheng, X. Yan, H. Xu, L. Shi, Sintering process as relevant parameter for Bi_2O_3 vaporization from $ZnO-Bi_2O_3$-based varistor ceramics, Transactions of Nonferrous Metals Society of China 19 (2009) 1526-1532

[14] J. T. S. Irvine, D. C. Sinclair, A. R. West, Electroceramics: Characterization by Impedance Spectroscopy, Advanced Materials 2 (3) (1990)132-138

[15] J. Xiang, Z. G. Liu, J. H. Ouyang, F. Y. Yan, Synthesis, structure and electrical properties of rare-earth doped apatite-type lanthanum silicates, Electrochimica Acta 65 (2012) 251-256

ANNEX 4

APATITE SAMPLES PRESENTED IN THE THESIS

Nr.	Reaction conditions			Thermal treatment			Theoretical formula of the final compound
	Molar report Nitrates :TEOS	Activator		Temp. (^{o}C)	Heating rate (^{o}C/min.)	Time (min.)	
		Cations	Concentration (%) [1]				
Synthesis method – Solid State Reaction							
1	1 : 0,60	Ce^{3+}-Tb^{3+}	1,5 - 1,5	1000	30	30	Ca$_2$Y$_{7,76}$Ce$_{0,12}$Tb$_{0,12}$(SiO$_4$)$_6$O$_2$
2				1100			
3				1200			
4				1300			
5				1400			
6	1 : 0,60	Ce^{3+}-Tb^{3+}	1,5 - 1,5	1200	3	30	Ca$_2$Y$_{7,76}$Ce$_{0,12}$Tb$_{0,12}$(SiO$_4$)$_6$O$_2$
7						120	
8						240	
9						480	

[1] *reported at 8 moles of Y*

Nr.	Host lattice	Activator		Thermal treatment		Theoretical formula of the final compound
		Cations	Conc. (%) [2]	Temperature (^{o}C)	Time (h)	
Synthesis method - Combustion						
10	La$_{10}$(SiO$_4$)$_6$O$_3$	Bi^{3+}	1,5	1200	4	La$_{9,85}$Bi$_{0,15}$(SiO$_4$)$_6$O$_3$
11	Y$_{10}$(SiO$_4$)$_6$O$_3$		1,5			Y$_{9,85}$Bi$_{0,15}$(SiO$_4$)$_6$O$_3$
12	Mg$_2$Y$_8$(SiO$_4$)$_6$O$_2$		1,0			Mg$_2$Y$_{7,92}$Bi$_{0,08}$(SiO$_4$)$_6$O$_2$
13	Ca$_2$Y$_8$(SiO$_4$)$_6$O$_2$		1,0			Ca$_2$Y$_{7,92}$Bi$_{0,08}$(SiO$_4$)$_6$O$_2$
14	Ca$_2$Y$_8$(SiO$_4$)$_6$O$_2$	Ce^{3+}	1,5	1400	4	Ca$_2$Y$_{7,85}$Ce$_{0,12}$(SiO$_4$)$_6$O$_2$
15		Tb^{3+}				Ca$_2$Y$_{7,85}$Tb$_{0,12}$(SiO$_4$)$_6$O$_2$
16		Eu^{3+}				Ca$_2$Y$_{7,85}$Eu$_{0,12}$(SiO$_4$)$_6$O$_2$
17		Ce^{3+}-Tb^{3+}	1,5 - 1,5			Ca$_2$Y$_{7,76}$Ce$_{0,12}$Tb$_{0,12}$(SiO$_4$)$_6$O$_2$ *
18		Ce^{3+}-Tb^{3+}-Eu^{3+}	1,5-1,5-1,5			Ca$_2$Y$_{7,64}$Ce$_{0,12}$Tb$_{0,12}$Eu$_{0,12}$(SiO$_4$)$_6$O$_2$

* *sample prepared S-G method too*

Nr.	Host lattice	Activator		Thermal treatment		Theoretical formula of the final compound
		Cations	Conc. (%)	Temperature (^{o}C)	Time (h)	
20	La$_{10}$(SiO$_4$)$_6$O$_3$	Bi^{3+}	0,25	1200	4	La$_{9,975}$Bi$_{0,025}$(SiO$_4$)$_6$O$_3$
21			0,50			La$_{9,95}$Bi$_{0,05}$(SiO$_4$)$_6$O$_3$
22			1,00			La$_{9,90}$Bi$_{0,10}$(SiO$_4$)$_6$O$_3$
23			1,50			La$_{9,85}$Bi$_{0,15}$(SiO$_4$)$_6$O$_3$
24			2,00			La$_{9,80}$Bi$_{0,20}$(SiO$_4$)$_6$O$_3$
25			3,00			La$_{9,70}$Bi$_{0,30}$(SiO$_4$)$_6$O$_3$
26	La$_{10}$(SiO$_4$)$_6$O$_3$	Bi^{3+}	0,0	1400	6	La$_{10}$(SiO$_4$)$_6$O$_3$
27			1,0			La$_{9,90}$Bi$_{0,10}$(SiO$_4$)$_6$O$_3$
28			1,5			La$_{9,85}$Bi$_{0,15}$(SiO$_4$)$_6$O$_3$
29			1,5	1500		La$_{9,85}$Bi$_{0,15}$(SiO$_4$)$_6$O$_3$
30			2,0	1400		La$_{9,80}$Bi$_{0,20}$(SiO$_4$)$_6$O$_3$
31			3,0			La$_{9,70}$Bi$_{0,30}$(SiO$_4$)$_6$O$_3$
32	La$_{10}$(SiO$_4$)$_6$O$_3$	Cr^{3+}	1,66 ♦	1400	6	La$_{10}$Si$_{5,9}$Cr$_{0,1}$O$_{26,95}$
33		Fe^{3+}				La$_{10}$Si$_{5,9}$Fe$_{0,1}$O$_{26,95}$
34		Mn^{4+}				La$_{10}$Si$_{5,9}$Mn$_{0,1}$O$_{27,00}$
35		Mo^{6+}				La$_{10}$Si$_{5,9}$Mo$_{0,1}$O$_{27,10}$
36		W^{6+}				La$_{10}$Si$_{5,9}$W$_{0,1}$O$_{27,10}$

♦ *the concentration is reported at 6 moles Si*

1 *Reported to* **RE= Y, La**

Nr.	Reaction conditions			Activator		Thermal regime		Theoretical formula of the final compound
	Precipitating Agent	Molar report Nitrates:TEOS	pH	Cations	Concentration (%) [2]	Temp. (°C)	Time (h)	
Synthesis method - *Microwave assisted Precipitation*								
37	$C_2H_2O_4$							
38	$C_6H_8O_7$							
39	CH_4N_2O	1 : 0,60	free	Ce^{3+}-Tb^{3+}	1,5 - 1,5	1200	1	$Ca_2Y_{7,76}Ce_{0,12}Tb_{0,12}(SiO_4)_6O_2$
40	NH_4OH							
41	NaOH							
42	Na_2CO_3							
43						800		
44						1100		
45						1200	4	$Ca_2Y_{7,88}Tb_{0,12}(SiO_4)_6O_2$
46						1300		
47	NaOH	1 : 0,60	free	Tb^{3+}	1,5	1400		
48						800		
49						1100		
50						1200	4	$Ca_2La_{7,88}Tb_{0,12}(SiO_4)_6O_2$
51						1300		
52						1400		
53					0,5			$Ca_2Y_{7,96}Ce_{0,04}(SiO_4)_6O_2$
54					1,5			$Ca_2Y_{7,88}Ce_{0,12}(SiO_4)_6O_2$
55	NaOH	1 : 0,60	free	Ce^{3+}	3,0	1400	4	$Ca_2Y_{7,76}Ce_{0,24}(SiO_4)_6O_2$
56					6,0			$Ca_2Y_{7,52}Ce_{0,48}(SiO_4)_6O_2$
57					9,0			$Ca_2Y_{7,28}Ce_{0,72}(SiO_4)_6O_2$
58		1 : 0,60						
59	NaOH	1 : 0,75	free	Ce^{3+}-Tb^{3+}	1,5 - 1,5	1400	4	$Ca_2Y_{7,76}Ce_{0,12}Tb_{0,12}(SiO_4)_6O_2$
60		1 : 0,81						
61		1 : 0,90						
Synthesis method - *Precipitation*								
62			7					
63	NaOH	1 : 0,60	9	Ce^{3+}-Tb^{3+}	1,5 - 1,5	1400	4	$Ca_2Y_{7,76}Ce_{0,12}Tb_{0,12}(SiO_4)_6O_2$
64			11					
65			free					
66			7					
67	NaOH	1 : 0,84	9	Ce^{3+}-Tb^{3+}	1,5 - 1,5	1400	4	$Ca_2Y_{7,76}Ce_{0,12}Tb_{0,12}(SiO_4)_6O_2$
68			11					
69			free					
70		1 : 0,60						
71	NaOH	1 : 0,81	11	Ce^{3+}-Tb^{3+}	1,5 - 1,5	1400	4	$Ca_2Y_{7,76}Ce_{0,12}Tb_{0,12}(SiO_4)_6O_2$
72		1 : 0,84						
73		1 : 0,87						

[2] *Reported to* **RE= Y, La**

ANNEX 5

CURRICULUM VITAE

1. **Name and surname**: IOANA MIHAELA PERHAIŢA (born MAIER)

2. **Date/ place of birth**: 14.02.1969, ALBA, Ocna-Mureş

3. **Nationality**: Romanian

4. **Studies**:

Institution	Babeş-Bolyai University of Cluj-Napoca, Faculty of Chemistry and Chemical Engineering			
Stage	1988-1992	1993-1997	2000-2001	2016-2020
Certificat	Secondary studies	Engineer	Master	PhD

5. **Scientific title**: Engineer

6. **Professional experience**:

Period	*Institution*	*Position*
2015 - prez.	Babeş-Bolyai University of Cluj-Napoca_	Engineer
2008 - 2015	*Raluca Ripan* Research Institute of Chemistry	Research Assistant
2005 - 2008	Iluna România Import-Export, Cluj-Napoca	Manager Assistant
1997 - 2005	S.C. CEROC S.A., Cluj-Napoca	Engineer
1992 - 1997		Technician
1988 - 1992	Institute for Research and Design of Technologies for Glass and Fine Ceramics, Bucharest, Cluj-Napoca subsidiary	Analyst

7. **Patents**: 2 (co-author)

8. **Scientific papers**: 58 (ISI)

9. **Foreign languages**: English (B1)

10. **Skills**: *Microsoft Word, Excel, OriginPro, PowerPoint, Paint*, *CorelDraw*

    Software: STAR^e, OMNIC, TriSTAR, WinLAB, Spectra Manager

11. **Experience in national/ international programs:** 9 research projects (member)

ANNEX 6

SCIENTIFIC ACTIVITY

<u>Scientific papers published on the topic of the doctoral thesis</u>:

1) <u>I. Perhaita</u>, L. E. Muresan, L. Barbu Tudoran, D. T. Silipas, G. Borodi, Synthesis of silicate apatite phosphors with enhanced luminescence via optimized precipitation technique through pH control, Journal of Sol-Gel Science and Technology 96 (2020) 498-510 (**IF 2019 = 2,008**) **Q₂**

2) <u>I. Perhaita</u>, L. E. Muresan, A. Nicoara, L. Barbu Tudoran, G. Borodi, L. M. Muresan, Morpho-structural and electrical characterization of Bi doped Apatite type lanthanum silicates prepared by gel combustion, Applied Physics A 126 (2020) 637 (**IF 2019 = 1,810**) **Q₃**

3) <u>I. Perhaita</u>, L. E. Muresan, D. T. Silipas, L. Barbu Tudoran, Comparative study on blue-turquoise silicate apatite phosphors prepared via different synthesis routes, Journal of Sol-Gel Science and Technology 89 (2019) 807-819 (**IF 2019 = 2,008**) **Q₂**

4) L. E. Muresan, <u>I. Perhaita</u>, D. Prodan, G. Borodi, Studies on terbium doped apatite phosphors prepared by precipitation under microwave conditions, Journal of Alloys and Compounds 755 (2018) 135-146 (**IF 2018 = 4,175**) **Q₁**

5) <u>I. Perhaita</u>, L. E. Muresan, D. T. Silipas, G. Borodi, Y. Karabulut, J. Garcia Guinea, M. Ayvacikli, N. Can, The role of calcination temperature on structural and luminescence behaviour of novel apatite-based $Ca_2Y_8(SiO_4)_6O_2$: Ce^{3+},Tb^{3+} phosphors, Applied Radiation and Isotopes 130 (2017) 188–197 (**IF 2017 = 1,123**) **Q₃**

Representative scientific papers published in the field of oxidic materials:

1. Tunable luminescence of broadband-excited and narrow line green emiting Y_2SiO_5:Ce^{3+}, Tb^{3+} phosphor, L. E. Muresan, Y. Karabulut, A. I. Cadis, I. Perhaita, A. Canimoglu, J. Garcia Guinea, L. Barbu- Tudoran, D. Silipas, M. Ayvacikli, N. Can, *Journal of Alloys and Compounds,* 658, 2016, 356-366 (**IF 2015 = 2,99**).
2. Rare earth activated yttrium aluminate phosphors with modulated luminescence, L. E. Muresan, E. J. Popovici, I. Perhaita, E. Indrea, J. Oro, N. Casan Pastor, *Luminescence*, 31(4), 2016, 929-936(**IF 2015 = 2,518**).
3. Optical spectroscopy of the Ce-doped multicomponent garnets, A. Canimoglu, Y. Karabulut, M. Ayvacikli, L. E. Muresan, I.Perhaita, L. Barbu-Tudoran, J. Garcia Guinea, T. Karali, N. Can, *Applied Radiation and Isotope*, 114, 2016, 114-120 (**IF 2015 = 1,136**).
4. Influence of vinyltriethoxysilane concentration on structural and luminescent characteristics of cerium doped yttrium based silicate phosphors; L. E. Muresan; A. I. Cadis; I. Perhaita; O. Ponta; O. Pana; L. Trinkler; B. Berzina; V. Korsaks, *Ceramics International*, 41(10), 2015, 13179-13188 (**IF 2014 = 2,605**).
5. Effect of ultrasound treatment on the morpho-structural and luminescent characteristics of cerium doped yttrium silicate phosphors, L. E. Muresan, A. I. Cadis, I. Perhaita, D.T. Silipas, L. Barbu Tudoran, *Material Research Bulletin,* 68, 2015, 295-301(**IF 2014= 2,288**).
6. Thermal behavior of precursors for synthesis of Y_2SiO_5:Ce phosphor via gel combustion , L. E. Muresan, A. I. Cadis, I. Perhaita, O. Ponta, D.T. Silipas, *Journal of Thermal Analysis and Calorimetry*, 119(3), 2015, 1565-1576 (**IF 2014 = 2,042**).
7. Studies on Y_2SiO_5:Ce phosphors prepared by gel combustion using new fuels, L. E. Muresan, B. F Oprea, A. I. Cadis, I. Perhaita, O. Ponta, *Journal of Alloys and Compounds,* 615, 2014, 795-803(**IF 2014 = 2,999**).
8. The influence of synthesis methods on the morpho-structural and luminescent characteristics of rare earth silicate phosphors, L.E. Muresan, A.I. Cadis, I. Perhaita, B.F. Oprea, D.T. Silipas, *AIP Conference Proceedings*, 1565, 2013, 193-198 .
9. Effect of the europium doping on the structural and luminescent properties of yttrium aluminum garnet, L. E. Muresan, E. J. Popovici, I. Perhaita, E. Indrea , T. D. Silipas, *Materials Science and Engineering B: Solid-State Materials for Advanced Technology*, 178(4), 2013, 248-253(**IF 2013 = 2,122**).
10. Investigation of thermal decomposition of yttrium-aluminum-based precursors for YAG phosphors, L. E. Muresan, E. J. Popovici, E. Bica, A. Cadis, I. Perhaita, L. B. Tudoran, *Journal of Thermal Analysis and Calorimetry*, 110(1), 2012, 341-348(**IF 2012 = 2,042**).

Patents:

1. Elisabeth-Jeanne Popovici, Adrian-Ionuţ Cadiş, Luminiţa Silaghi-Dumitrescu, Ioana Mihaela Perhaiţa, *A process for the preparation of nanocrystalline zinc sulfide*, RO 127954 B1/ 2016.
2. Laura Elena Mureşan, Adrian-Ionuţ, Cadiş Ioana Mihaela Perhaiţa, *A process for the preparation of luminescent pigments based on yttrium silicate doped with rare earth ions with variable luminescence,* RO 132148 B1/ 2020.

Research projects:

1. A support tool model for decision making to reduce the health risk associated with the uncontrolled water and food sources in rural Roma communities in Transylvania - *RomaHealthRisk* (RO-NO-2019-0463), Project manager: Dr. M. S. Beldean-Galea, 2020-2022.
2. Functional collaboration model between public research organizations and the economic environment in order to provide high-level scientific and technological services in the field of bioeconomy (PN-III-P1-1.2-PCCDI-2017-0056), Project manager: Dr. D. C. Vodnar, 2018-2020.
3. New luminescent core/shell sulfide-based nano-materials - *LUNAMACOSH* (TE-2014-4-1391), Project manager: Dr. A. I. Cadiş, 2015-2017.
4. Yttrium silicate nanoluminophores for optoelectronics (PN-II-RU-TE-2012-3-0360), Project manager: Dr. L. E. Mureşan, 2012-2016.
5. Bio-medical applications of metal compounds - *METALLOMIX* (PN-II-ID-PCCE-2008-1-140), Project manager: Acad. I. Haiduc, 2010-2012.
6. Physico-chemical aspects regarding the synthesis of micro- and nanostructured luminescent materials with controlled properties - *MATERLUM* (D-2488/ctr.710), Project manager: Dr. E. J. Popovici, 2009-2011.
7. Micro and nanostructured oxidic materials with controlled luminescent chromatics for lighting devices - *MAMINAL* (PN2 71-122), Project manager: Dr. L. E. Mureşan, 2007-2010.
8. Calixarene-based materials with recognition properties of some ionic and molecular species for biological and ecological interest - *CALIXMAT* (PN2 71-062), Director proiect: Dr. E. J. Popovici, 2007-2010.
9. Composite materials based on metal-oxide clusters with Dawson structure for selective oxidation of terpenes - *POLIOXO* (ID-687), Project manager: Dr. R. Tomsa, 2007-2009.